RESEARCH ARTICLE

Endogenous Retroelement Activation by Epigenetic Therapy Reverses the Warburg Effect and Elicits Mitochondrial-Mediated Cancer Cell Death

Vicente Fresquet[1], Maria J. Garcia-Barchino[1], Marta Larrayoz[1], Jon Celay[1], Carmen Vicente[1], Marta Fernandez-Galilea[1,2], Maria J. Larrayoz[1], Maria J. Calasanz[1], Carlos Panizo[3], Alexandra Junza[4], Jiahuai Han[5], Celia Prior[6], Puri Fortes[6], Ruben Pio[7], Julen Oyarzabal[8], Alvaro Martinez-Baztan[1], Bruno Paiva[1], Maria J. Moreno-Aliaga[2], Maria D. Odero[1], Xabier Agirre[1], Oscar Yanes[4], Felipe Prosper[1,3], and Jose A. Martinez-Climent[1]

Illustration by Bianca Dunn

ABSTRACT For millions of years, endogenous retroelements have remained transcriptionally silent within mammalian genomes by epigenetic mechanisms. Modern anticancer therapies targeting the epigenetic machinery awaken retroelement expression, inducing antiviral responses that eliminate tumors through mechanisms not completely understood. Here, we find that massive binding of epigenetically activated retroelements by RIG-I and MDA5 viral sensors promotes ATP hydrolysis and depletes intracellular energy, driving tumor killing independently of immune signaling. Energy depletion boosts compensatory ATP production by switching glycolysis to mitochondrial oxidative phosphorylation, thereby reversing the Warburg effect. However, hyperfunctional succinate dehydrogenase in mitochondrial electron transport chain generates excessive oxidative stress that unleashes RIP1-mediated necroptosis. To maintain ATP generation, hyperactive mitochondrial membrane blocks intrinsic apoptosis by increasing BCL2 dependency. Accordingly, drugs targeting BCL2 family proteins and epigenetic inhibitors yield synergistic responses in multiple cancer types. Thus, epigenetic therapy kills cancer cells by rewiring mitochondrial metabolism upon retroelement activation, which primes mitochondria to apoptosis by BH3-mimetics.

SIGNIFICANCE: The state of viral mimicry induced by epigenetic therapies in cancer cells remodels mitochondrial metabolism and drives caspase-independent tumor cell death, which sensitizes to BCL2 inhibitor drugs. This novel mechanism underlies clinical efficacy of hypomethylating agents and venetoclax in acute myeloid leukemia, suggesting similar combination therapies for other incurable cancers.

INTRODUCTION

Epigenetic inhibitors of DNA methyltransferases (DNMT) and histone deacetylases (HDAC) constitute a standard-of-care treatment in patients with leukemia, lymphoma, and multiple myeloma (1). In addition, drugs targeting various histone methyltransferases (HMT) are undergoing clinical trials in patients with different tumor types (2). Despite approval, clinical efficacy of epigenetic drugs as single agents has been moderate, pointing us to pursue combination with other drugs to treat patients with cancer more effectively (1, 2). It is therefore mandatory to unravel the mechanisms underlying how epigenetic agents drive tumor cell death and sensitize tumor cells to other anticancer agents.

Epigenetic inhibitors impair survival of cancer cells by reactivating transcriptionally silenced tumor-suppressor genes, by reversing the acquired DNA methylation of cancer cells, and by targeting specific gain-of-function mutations in epigenetic enzymes (1, 2). In addition, epigenetic inhibitors of DNMT, HDAC, and HMT enzymes eliminate cancer cells by awakening widespread transcription of endogenous retroelements (3, 4). Among retroelements, endogenous retroviruses (ERV) are remnants of ancestral germline viral infections integrated within the human genome, which have remained silent by multiple layers of the epigenetic machinery to prevent deleterious expression (5–7). Active retroelement transcription generates double-stranded RNAs (dsRNA) in tumor cells, which react as if being infected by an exogenous virus and thereby mount innate antiviral immune responses by promoting IFN signaling that leads to tumor cell death (3, 4, 8, 9). Such a state of viral mimicry also boosts tumor immunogenicity, which implements T cell–mediated efficacy of immune checkpoint inhibitors (4, 10–12). Accordingly, epigenetic agents in combination with anti–PD-1 or PD-L1 inhibitors are currently being tested in clinical trials in a variety of tumor types (13, 14).

We have developed a series of epigenetic drug inhibitors targeting DNMTs and the G9a HMT with potent antitumor activity (15). In *in vivo* cancer cell models, the dual epigenetic inhibitors reactivated endogenous retroelements and increased tumor immunogenicity, which sensitized tumor cells to the effects of immune checkpoint blockade (16).

---

[1]Division of Hematology, Center for Applied Medical Research CIMA, University of Navarra, IDISNA, CIBERONC, Pamplona, Spain. [2]Center for Nutrition Research and Department of Nutrition, Food Science and Physiology, University of Navarra, IDISNA, CIBEROBN, Pamplona, Spain. [3]Department of Hematology, Clinica Universidad de Navarra, University of Navarra, IDISNA, CIBERONC, Pamplona, Spain. [4]Universitat Rovira i Virgili, Department of Electronic Engineering, IISPV, CIBERDEM, Tarragona, Spain. [5]State Key Laboratory of Cellular Stress Biology, Innovation Center for Cell Signaling Network, School of Life Sciences, Xiamen University, Xiamen, Fujian, China. [6]Division of Gene Therapy and Hepatology, Center for Applied Medical Research CIMA, University of Navarra, IDISNA, CIBEREHD, Pamplona, Spain. [7]Division of Solid Tumors, Center for Applied Medical Research CIMA, University of Navarra, IDISNA, CIBERONC, Pamplona, Spain. [8]Division of Molecular Therapeutics, Center for Applied Medical Research CIMA, University of Navarra, IDISNA, Pamplona, Spain.

Note: Supplementary data for this article are available at Cancer Discovery Online (http://cancerdiscovery.aacrjournals.org/).

M.J. Garcia-Barchino, M. Larrayoz, and J. Celay contributed equally to this article.

Corresponding Authors: Jose A. Martinez-Climent, Division of Hematology, Center for Applied Medical Research (CIMA), School of Medicine, University of Navarra, Avda. Pio XII, 55, 31008 Pamplona, Spain. Phone: 34-948-194700, ext. 811029; Fax: 34-948-194714; E-mail: jamcliment@unav.es; and Vicente Fresquet, vfresquet@unav.es

Cancer Discov 2021;11:1268–85

doi: 10.1158/2159-8290.CD-20-1065

However, the tumor cell–intrinsic mechanisms underlying immunogenic death following epigenetic targeting are not well characterized. Based on our own preliminary results and on previous observations (17, 18), we hypothesized that the state of viral mimicry induced by epigenetic therapy promotes tumor cell death by cell-autonomous mechanisms independently of IFN-mediated immune responses.

RESULTS

Epigenetically Driven Retroelement Activation Induces RIP1-Mediated Tumor Necroptosis

To investigate whether endogenous retroelement transcription induces tumor cell death at the cell-intrinsic level, a series of cell lines derived from patients with common hematologic malignancies and solid tumors were exposed to different epigenetic agents. Following *in vitro* treatment, a strong increase in the expression of ERV transcripts was observed for six drugs targeting DNMTs, HDACs, or HMTs used at their IC_{50} (Fig. 1A; Supplementary Table S1). Such a massive amount of dsRNAs was detected by confocal microscopy in the cytoplasm of tumor-treated cells (Fig. 1B). To define the consequences of the viral gene reactivation, we focused on two representative compounds targeting proteins from the principal epigenetic families: CM272, the lead compound in our series of dual DNMT and HMT inhibitors (15, 16), and the clinically approved HDAC inhibitor vorinostat (19). A marked, dose-dependent increase in ERV transcription was observed using both compounds at IC_{25}, IC_{50}, and IC_{75} doses in all studied hematopoietic and solid neoplasms (Fig. 1C and D; Supplementary Fig. S1A and S1B). Following ERV activation, dose-dependent increase in the expression of the genes encoding the RIG-I and MDA5 helicases, the main cytosolic sensors of RNA viruses which are activated to limit viral replication (20), was detected in tumor cells (Fig. 1C–E; Supplementary Fig. S1A and S1C). Dose-dependent oligomerization of MAVS protein, which transduces signals from viral–helicase complexes to activate IFN responses (21), was observed in treated cells (Fig. 1F). Accordingly, a dose-dependent increase in the expression of IFN-stimulated genes (ISG) was found after treatment (Fig. 1C and D; Supplementary Fig. S1A). Additional studies revealed that the expression levels of ERV genes, the helicase-coding RIG-I and MDA5 genes, and ISGs strongly correlated with tumor cell viability following treatment (Fig. 1G; Supplementary Fig. S1D). Thus, DNMT, HDAC, and HMT inhibitors trigger common antiviral responses that correlate with cell death, which supports a role of endogenous retroelements in cell-autonomous tumor killing.

Investigation of the mechanisms underlying tumor cell death revealed that epigenetic agents induce a dose-dependent increase of late Annexin V–expressing cells and PARP cleavage, but changes in the expression of apoptosis proteins including cleavage of caspases 3, 8, and 9, which is the hallmark of apoptosis (22), were observed only at high doses (Fig. 2A; Supplementary Fig. S2A and S2B). Assessment of nonapoptotic cell death types following epigenetic therapies excluded changes in autophagy-related proteins, but a consistent increased phosphorylation of RIP1, RIP3, and MLKL kinases, which is the biochemical hallmark of activated necroptosis (23), was observed (Fig. 2A–C; Supplementary Fig. S2C). Accordingly, electron microscopy identified typical ultrastructural features of necroptosis in treated tumor cells, including cell membrane rupture, cytoplasm vacuolization, and swelled mitochondria, without evident signs of apoptosis (Fig. 2D). Moreover, the pharmacologic inhibition of RIP1, RIP3, or MLKL reduced drug-induced cell death, whereas it was reversed to a lesser extent with the pan-caspase inhibitor z-VAD (Fig. 2E; Supplementary Fig. S2D). Confirming these findings, several cell line models with CRISPR/Cas9 genetic ablation of RIP1, RIP3, or MLKL showed diminished cell death rates after epigenetic therapy in comparison with wild-type cells (Fig. 2F; Supplementary Fig. S2E). Further linking endogenous retroelement activation and tumor cell death, mimicking dsRNA formation by administering poly(I:C) into tumor cells reproduced epigenetic drug–induced antiviral responses leading to RIP1-mediated necroptosis (Fig. 2G). In sum, epigenetic drugs target cancer cells by primarily inducing caspase-independent, RIP-mediated necroptosis.

Recognition of Endogenous Retroelements by RIG-I and MDA5 Helicases Depletes Intracellular ATP

To further investigate the mechanism of drug-induced necroptosis in tumor cells, two patient-derived cell lines from acute myeloid leukemia (AML) and hepatocellular carcinoma (HCC) with genetic deletion of the RIG-I and MDA5 helicases, MAVS, and the IRF3 or IRF7 components of the IFN cascade were treated with epigenetic agents (Fig. 3A). Following ERV transcriptional activation, reduced expression of ISGs was observed in tumor cells with genetic ablation of the helicases with respect to wild-type cells, which was accompanied by increased cell viability rates (Fig. 3B and C; Supplementary Fig. S3A and S3B). In contrast, in AML and HCC cells with genetic deletion of MAVS, cell death rates were not diminished with respect to control cells, despite the marked reduction of ISG expression that was present after treatment (Fig. 3B and C). In line with these results, tumor cells with CRISPR/Cas9 deletion of IRF3 or IRF7 treated with epigenetic drugs showed similar cell death rates to wild-type cells, despite the reduced ISG expression that was detected (Fig. 3B). Moreover, administration of soluble IFN or pharmacologic blockade of IFN signaling in tumor cells in culture did not modify the cell death rates induced by epigenetic therapies (Supplementary Fig. S3C). These results indicate that epigenetically driven tumor cell death relies on the recognition of endogenous retroelement transcripts by RIG-I and MDA5 helicases, and not on downstream MAVS or IFN immune responses.

Because RIG-I and MDA5 catalyze the hydrolysis of ATP into ADP upon binding to viral dsRNAs (24, 25), we hypothesized that the massive helicase activation could be consuming ATP and promoting tumor cell death. This would link with our previous findings, because low intracellular ATP levels commonly shift the balance of programmed cell death toward necroptosis instead of apoptosis (26). In line with this notion, tumor cells treated with epigenetic agents showed a significant dose-dependent ATP reduction leading to increased ADP/ATP ratios (Fig. 3E; Supplementary Fig. S3D and S3E). Supporting the implication of energy metabolism in tumor killing, addition of glucose to cultured cells as an ATP source decreased death rates upon epigenetic drug exposure, whereas glucose depletion in the culture medium increased antitumor drug effects (Fig. 3E). Next, whether the helicases were directly

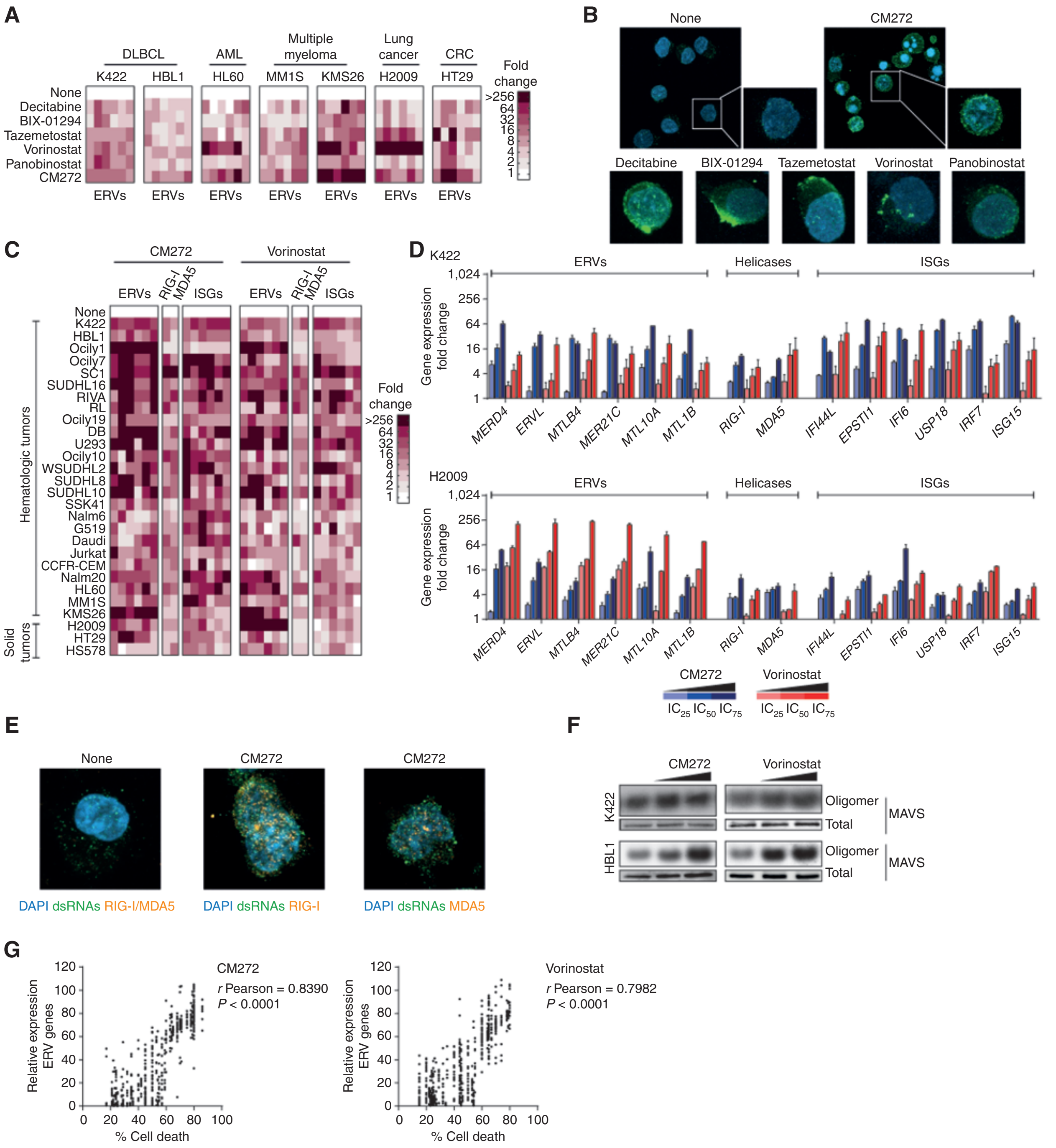

Figure 1. Epigenetic therapies induce common antiendogenous retroelement responses that correlate with tumor cell death. **A,** Heat map representation of the expression of six ERV genes (*MERD4, ERVL, MTLB4, MER21C, MTL10A,* and *MTL1B*) measured by qRT-PCR in cancer cell lines derived from patients with diffuse large B-cell lymphoma (DLBCL), acute myeloid leukemia (AML), multiple myeloma, and solid tumors [lung cancer and colorectal carcinoma (CRC)]. Fold changes represent the differences from untreated versus 24 hours after treatment with six epigenetic drugs at their IC_{50} dose. **B,** Confocal microscopic analysis of dsRNA expression using the J2 antibody in tumor cells before and after 24-hour treatment with six epigenetic drugs at their IC_{50} dose. **C,** Heat map illustration of the relative expression of ERV genes (*MERD4, ERVL, MTLB4, MER21C, MTL10A,* and *MTL1B*), helicase-coding genes (*RIG-I* and *MDA5*), and ISGs (*IFI44L, EPSTI1, IFI6, USP18, IRF7,* and *ISG15*) measured by qRT-PCR in tumor cell lines treated with CM272 and vorinostat at IC_{50} during 24 hours. Fold changes represent the differences in expression in untreated versus treated cells. **D,** Mean relative expression of ERV genes, helicases, and ISGs measured by qRT-PCR in K422 (DLBCL) and H2009 (lung cancer) cell lines treated with CM272 or vorinostat at their IC_{25}, IC_{50}, and IC_{75} doses. Fold changes represent the differences from untreated versus 24 hours after treatment. **E,** Immunofluorescence analyses to visualize dsRNA, RIG-I, and MDA5 expression in K422 cells untreated and treated with CM272 at IC_{50} dose during 24 hours. **F,** Western blot analysis of two DLBCL cell lines (K422 and HBL1) treated with CM272 and vorinostat during 24 hours. MAVS oligomerization and total MAVS expression were determined in untreated and treated cells using IC_{25} and IC_{50} dose of the drugs. **G,** Correlation plots showing the relative expression changes of ERV genes with the percentage of tumor cell death in 28 cell lines treated during 24 hours with increasing doses of CM272 and vorinostat.

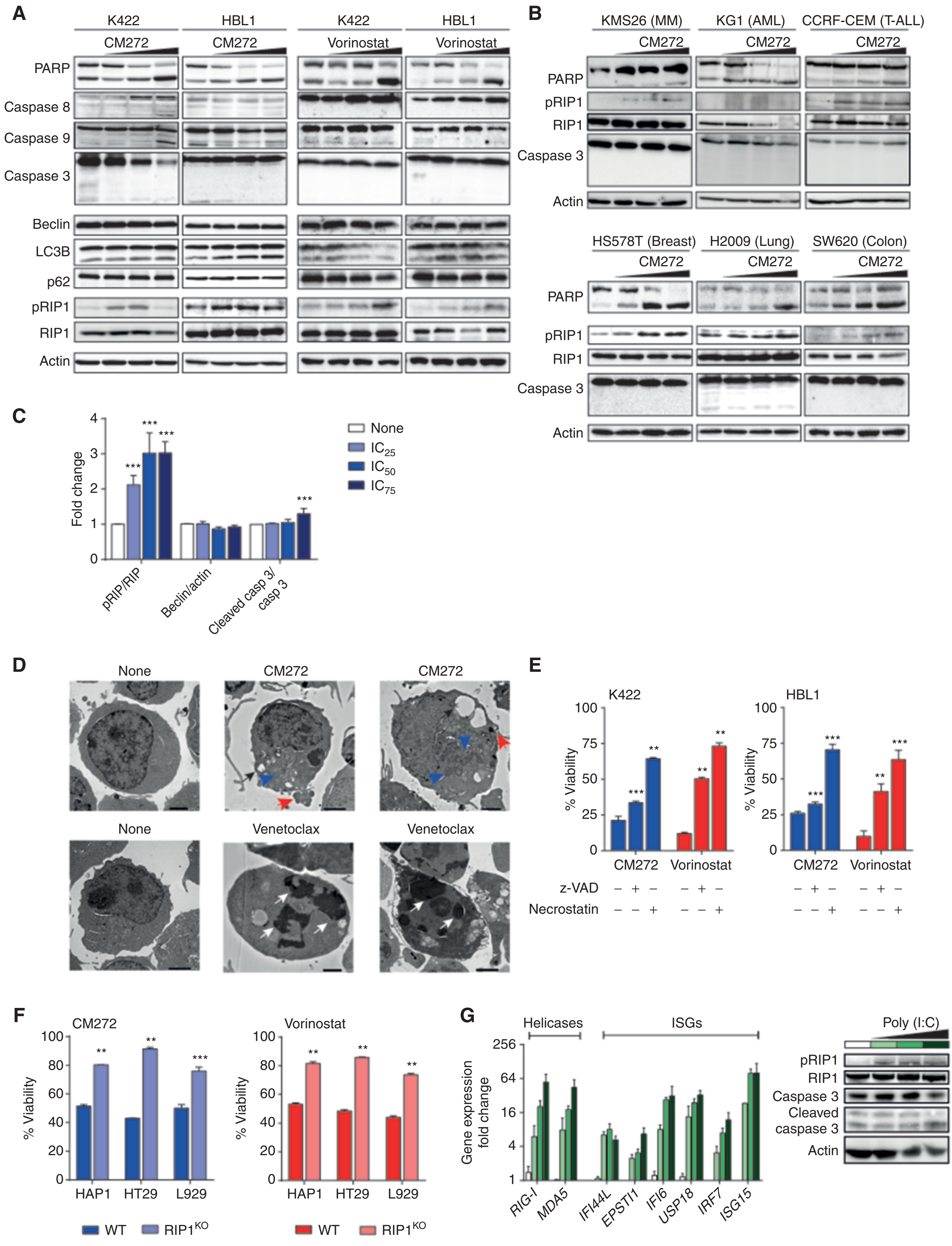
A
K422
HBL1
K422
HBL1
CM272
CM272
Vorinostat
Vorinostat
PARP
Caspase 8
Caspase 9
Caspase 3
Beclin
LC3B
p62
pRIP1
RIP1
Actin
B
KMS26 (MM)
KG1 (AML)
CCRF-CEM (T-ALL)
CM272
PARP
pRIP1
RIP1
Caspase 3
Actin
HS578T (Breast)
H2009 (Lung)
SW620 (Colon)
CM272
PARP
pRIP1
RIP1
Caspase 3
Actin
C
Fold change
0
1
2
3
4
***
***
***
***
pRIP/RIP
Beclin/actin
Cleaved casp 3/ casp 3
None
IC25
IC50
IC75
D
None
CM272
CM272
None
Venetoclax
Venetoclax
E
K422
HBL1
% Viability
100
75
50
25
0
CM272
Vorinostat
z-VAD – + – – + –
Necrostatin – – + – – +
**
***
**
**
***
***
**
***
F
CM272
Vorinostat
% Viability
100
80
60
40
20
0
HAP1
HT29
L929
WT
RIP1KO
**
**
***
**
**
**
G
Helicases
ISGs
Gene expression fold change
256
64
16
4
1
RIG-I
MDA5
IFI44L
EPSTI1
IFI6
USP18
IRF7
ISG15
Poly (I:C)
pRIP1
RIP1
Caspase 3
Cleaved caspase 3
Actin

modulating energy metabolism was assessed. In contrast to the ATP depletion leading to high ADP/ATP ratios observed in wild-type controls, AML and HCC cells with deletion of RIG-I/MDA5 showed minor increases in the ADP/ATP ratio following epigenetic therapies (Fig. 3F). Consistently, external supply or deprivation of glucose in RIG-I/MDA5-deficient cells did not change cell death rates following therapy (Fig. 3G). In contrast, in cells with deletion of MAVS, IRF3, or IRF7, epigenetic therapies increased the ADP/ATP ratios at similar levels to those observed in wild-type cells, and glucose administration or deprivation induced comparable cell death rate changes in deleted versus wild-type cells (Fig. 3F and G). These data indicate that ATP depletion relies on RIG-I and MDA5 helicase function, and not on MAVS or IFN signaling. To further demonstrate a causative role of the helicases in energy consumption by hydrolyzing ATP through their ATPase catalytic domains, expression of RIG-I and MDA5 wild-type or ATPase mutant plasmids (which impede ATP hydrolysis) was performed in RIG-I–deficient and MDA5-deficient cells, respectively (27, 28). Wild-type helicase reexpression restored the increased ATP consumption and enhanced cell death rates upon drug exposure. However, these effects were not observed after transfection of RIG-I–expressing or MDA5-expressing plasmids carrying mutations in ATP catalytic domains (Fig. 3H). Thus, endogenous retroelement recognition by the helicases increases ATP hydrolysis and depletes intracellular energy, which modulates tumor cell death independently of the IFN response.

Energy Depletion Promotes the Reversion of the Warburg Effect

The metabolic consequences of drug-induced energy depletion were next investigated. At basal conditions, tumor cell lines exhibited the typical Warburg effect, defined by an aerobic glycolytic state [shown by increase in the extracellular acidification rate (ECAR)] with limited mitochondrial oxidative phosphorylation [OXPHOS; shown by low oxygen consumption rate (OCR); Fig. 4A and B; Supplementary Fig. S4A; ref. 29]. Epigenetic therapies minimally increased ECAR, and time-course measurement of lactate extrusion revealed a decrease over time, indicating that glycolysis was being progressively limited (Fig. 4A and C). On the contrary, marked dose-dependent increase in OCR was observed upon epigenetic therapy, indicating the activation of OXPHOS (Fig. 4B and D). Because OXPHOS produces 18 times more molecules of ATP than glycolysis (29), these results suggest that epigenetic drugs switch tumor cell metabolism from glycolysis to OXPHOS to maximize ATP generation in mitochondria, thereby reversing the Warburg effect. Supporting this notion, increased production of total ATP was observed in treated cells at the expense of mitochondrial ATP, whereas the levels of glycolytic ATP remained constant (Fig. 4E). To investigate how energy depletion activated OXPHOS, several energetic sensors including AMP-activated protein kinase were studied; however, we did not observe consistent changes in tumor cells after epigenetic drug exposure (Supplementary Fig. S4B). Given that viral RNA infections can assemble the RIP1–RIP3 necroptosome complex (30), which besides regulating necroptosis involves prosurvival cell functions leading to the activation of mitochondrial respiration (31, 32), we asked whether the necroptosome could be regulating the OXPHOS switch following endogenous retroelement expression. In time-course assays, the marked increase in OCR triggered by epigenetic therapies in wild-type tumor cells was not observed in cell lines with genetic ablation of RIP1 (Fig. 4F; Supplementary Fig. S4C). The lack of OCR triggering was also evident in tumor cells with RIP3 deletion treated with epigenetic drugs (Fig. 4F). Thus, targeting the epigenome reverses the Warburg effect through assembling the RIP necroptosome, with the aim of maximizing ATP generation in mitochondria.

Epigenetic Therapies Increase Tricarboxylic Acid Cycle Function Leading to Succinate Depletion

Next, the potential effects of epigenetic drugs on the tricarboxylic acid (TCA) cycle, which catabolizes glucose, amino acids, and fatty acids to generate ATP in mitochondria, were evaluated (Fig. 4G). Treatment of tumor cells increased the enzymatic activity of pyruvate dehydrogenase (PDH) complex, which catalyzes the conversion of pyruvate into acetyl coenzyme A, leading to an increase in the oxidation of glucose (Fig. 4H; Supplementary Fig. S4D). In addition, increased enzymatic activity of glutamate dehydrogenase 1 (GLUD1), the enzyme that catalyzes the conversion of glutamate into α-ketoglutarate, was observed, along with augmented uptake of the amino acid glutamate after treatment (Fig. 4H). Such increase in the use of glucose and glutamine was not observed in RIP1-deficient cells, indicating that the necroptosome regulated TCA cycle function upon epigenetic drug exposure (Supplementary Fig. S4E). However, variable increases in the uptake and oxidation of fatty acids were detected upon epigenetic therapy, indicating a limited role in the metabolic switch (Supplementary Fig. S4F). Then, quantification of the TCA cycle metabolites was next performed

Figure 2. Epigenetic therapies promote caspase-independent, RIP1-mediated tumor cell necroptosis. **A,** Western blot analyses of PARP cleavage, caspases 8, 9, and 3 (apoptosis-related proteins), beclin, LC3B, and p62 (autophagy-related proteins), and phosphorylated and total RIP1 (necroptosis-related protein) in untreated K422 and HBL1 cells and after treatment with CM272 and vorinostat during 24 hours at IC$_{25}$, IC$_{50}$, and IC$_{75}$ doses. **B,** Western blot analyses of PARP cleavage, phosphorylated versus total RIP1, and caspase 3 cleavage in cell lines from multiple myeloma (MM; KMS26), AML (KG1), T-cell acute lymphoblastic leukemia (T-ALL; CCRF-CEM), and breast (HS578), lung (H2009), and colon (SW620) cancer cell lines treated with CM272 at IC$_{25}$, IC$_{50}$, and IC$_{75}$ doses during 24 hours. **C,** Quantification of Western blot protein bands for phosphorylated RIP1 versus total RIP1, Beclin versus actin, and cleaved caspase 3 versus total caspase 3 shown in **A** and **B** by using the ImageJ software. **D,** Electron microscopy analysis of HBL1 cells treated for 24 hours with CM272 or the BCL2 inhibitor venetoclax at IC$_{50}$ doses. Epigenetic therapy induced morphologic signs of necroptosis, including cell membrane rupture (marked by red arrows), cytoplasm vacuolization (black arrows), and swelled mitochondria (blue arrows), whereas venetoclax promoted typical signs of apoptosis (white arrows), including pyknotic and shrunken nuclei with condensed cytoplasm. **E,** Changes in cell viability of tumor cell lines treated with CM272 and vorinostat at IC$_{50}$ doses, incubated with the RIP1 inhibitor necrostatin or the pan-caspase inhibitor z-VAD during 24 hours. **F,** Changes in cell viability of tumor cell lines with RIP1 deletion versus wild-type (WT) cells after treatment with CM272 at IC$_{50}$. HAP1, AML cells; HT29, colon cancer cells; and L929, tumorigenic fibroblasts. **G,** Effects of polyinosinic:polycytidylic acid [poly(I:C)] administration into K422 cells (which mimics dsRNA expression) promotes dose-dependent cell death with increased expression of helicase-coding genes and ISGs, and RIP1 phosphorylation. **, $P < 0.01$; ***, $P < 0.001$; nonsignificant (n.s.) values are not shown.

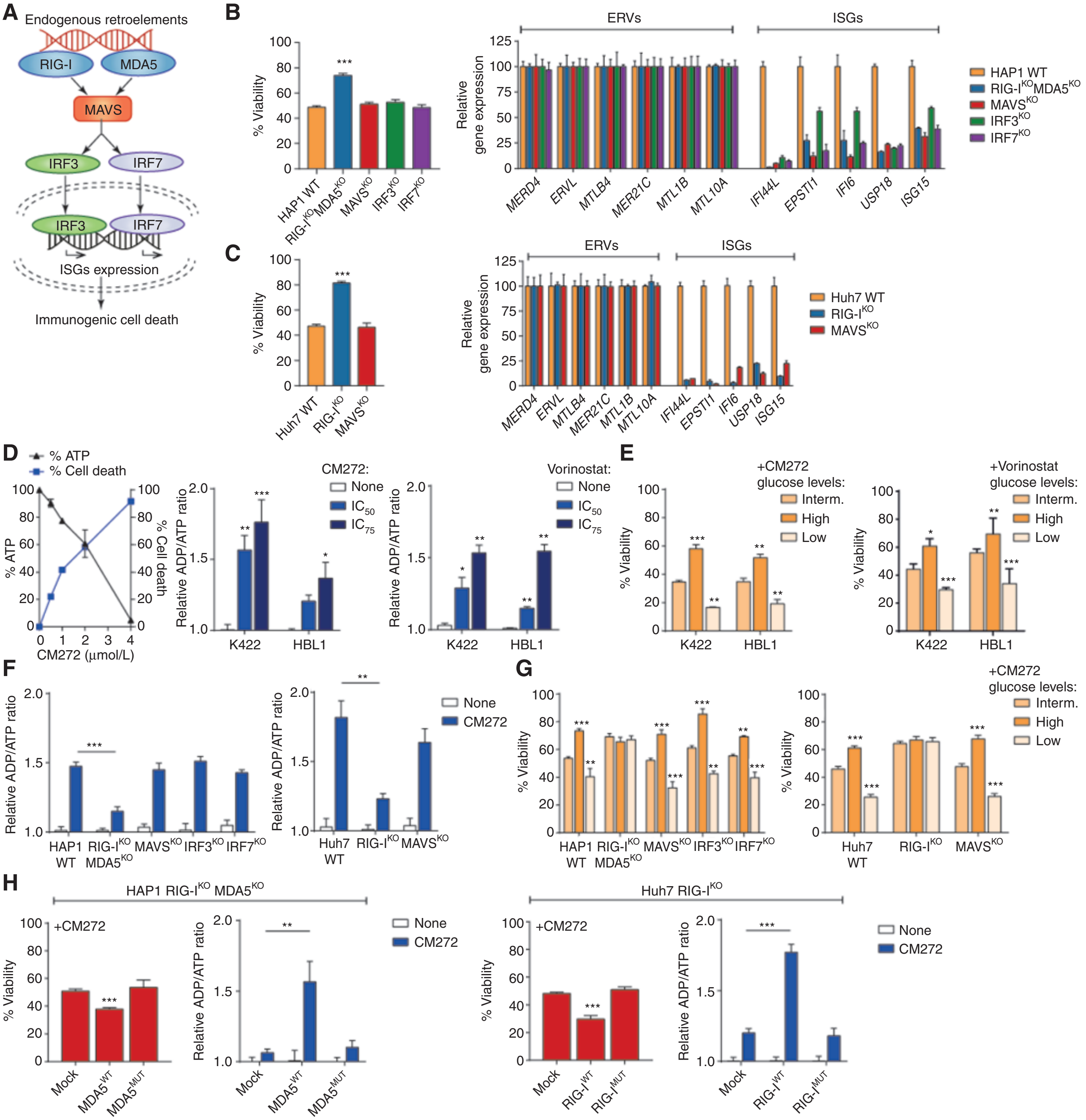

Figure 3. Endogenous retroelement recognition by the RIG-I and MDA5 helicases depletes intracellular ATP and modulates tumor cell death. **A,** Schematic representation of the antiendogenous retroelement response pathway, including the RIG-I and MDA5 helicases, MAVS, and IRF3 and IRF7, which lead to IFN-mediated responses. **B,** Epigenetic therapy in the wild-type (WT) AML cell line HAP1 and in HAP1-derived mutant cell lines carrying genetic inactivation of RIG-I and MDA5 (RIG-I/MDA5^{KO}), MAVS (MAVS^{KO}), IRF3 (IRF3^{KO}), and IRF7 (IRF7^{KO}) genes. On the left, viability of parental and mutant HAP1 cells after treatment with CM272 at IC$_{50}$. On the right, average fold changes in the expression of ERV genes and ISGs in parental and mutant HAP1 cells (normalized to HAP1 wild-type expression levels) after treatment with CM272 at IC$_{50}$ dose. Genetic deletions were confirmed by Western blot analyses. **C,** Epigenetic therapy in the Huh7 HCC cell line and in Huh7 cells with deletion of RIG-I (RIG-I^{KO}) and MAVS (MAVS^{KO}) genes. On the left, viability of parental and mutant Huh7 cells after treatment with CM272 at IC$_{50}$. On the right, average fold changes in the expression of ERV genes and ISGs in parental and mutant Huh7 cells after treatment with CM272 at IC$_{50}$ dose. Genetic deletions were confirmed by Western blot analyses. **D,** Measurement of dose-dependent ATP depletion in K422 and HBL1 cell lines leading to increase in ADP/ATP ratios in tumor cells treated with CM272 and vorinostat at IC$_{50}$ doses. **E,** Changes in cell viability in K422 and HBL1 cells cultured with low (1.2 mmol/L), intermediate (12.5 mmol/L), and high (60 mmol/L) concentration levels of glucose after treatment with CM272 and vorinostat during 24 hours at IC$_{50}$ doses. **F,** Changes in ADP/ATP ratios in HAP1 and Huh7 wild-type and mutant cell lines treated with epigenetic drugs at IC$_{50}$ dose. **G,** Cell viability of HAP1 and Huh7 wild-type and mutant cell lines treated with epigenetic drugs at IC$_{50}$ dose grown in culture media with low (1.2 mmol/L), intermediate (12.5 mmol/L), and high (60 mmol/L) glucose levels. **H,** Representation of cell viability and ADP/ATP ratios in HAP1 and Huh7 mutant cell lines transfected with wild-type or ATPase mutant plasmids after treatment with CM272. RIG-I/MDA5^{KO} HAP1 cells were transfected with wild-type MDA5 or mutant plasmids, whereas wild-type RIG-I or mutant plasmids were transfected into RIG-I^{KO} Huh7 cells. *, $P < 0.05$; **, $P < 0.01$; ***, $P < 0.001$.

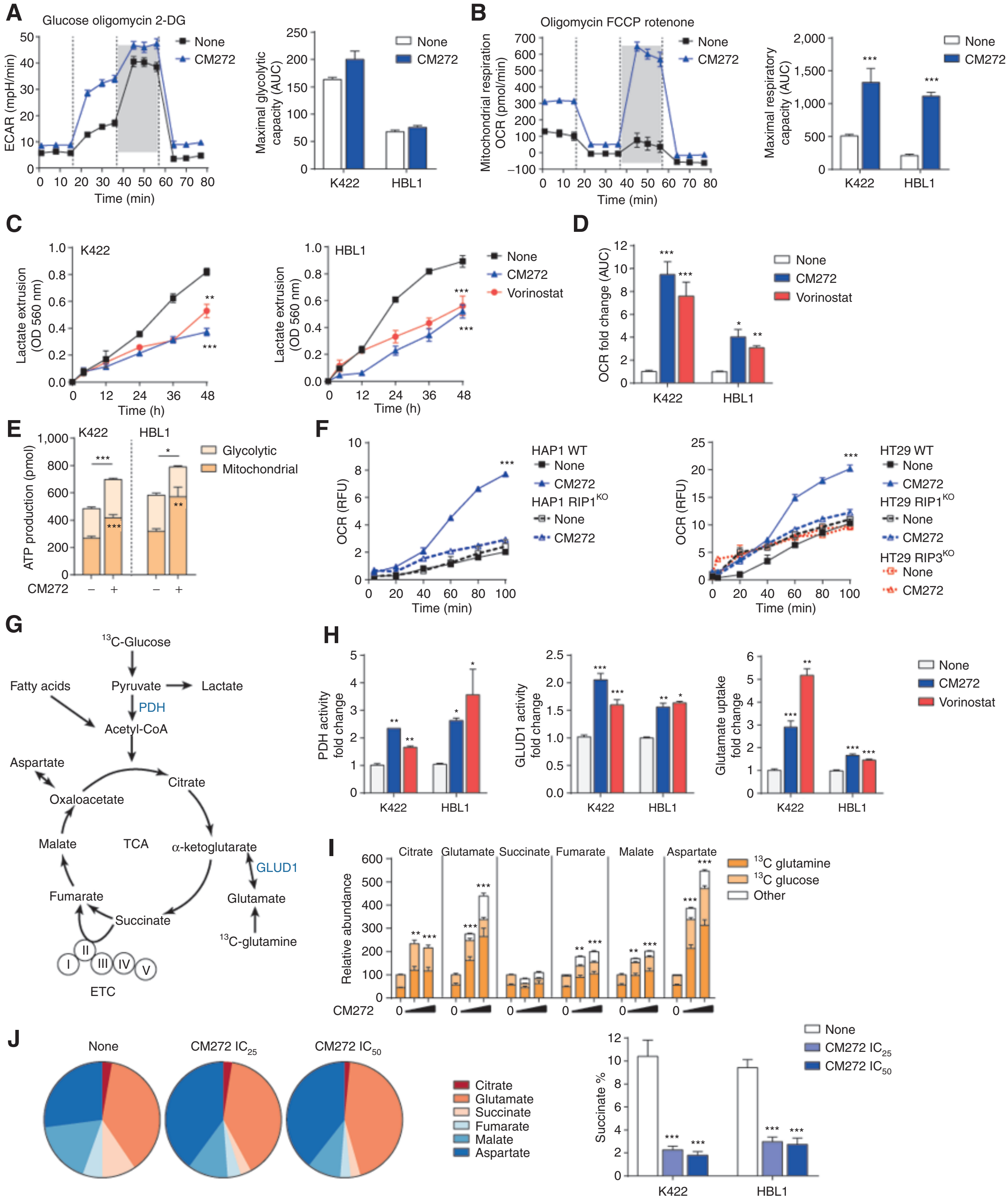

Figure 4. Reversion of the Warburg effect is driven by RIP1–RIP3 necroptosome, which increases TCA cycle catabolism and depletes succinate. **A,** Seahorse extracellular flux analysis in HBL1 cells shows dynamic representation of ECAR in HBL1 cells at basal condition and after 24-hour treatment with CM272. On the right, comparison of the maximal glycolytic capacity in HBL1 and K422 cells untreated versus treated with CM272. **B,** Seahorse extracellular flux analysis shows dynamic representation of OCR in HBL1 cells under basal condition and after CM-272 treatment. On the right, comparison of the maximal respiratory capacity in HBL1 and K422 cells after CM272 treatment. **C,** Time-course measurement of lactate extrusion in untreated versus treated cells CM272 and vorinostat during 48 hours at their IC_{50} doses. **D,** Treatment with CM272 and vorinostat during 24 hours at IC_{50} dose increases OCR in tumor cells. **E,** Quantification of glycolytic and mitochondrial ATP production following epigenetic therapy with CM272 in K422 and HBL1 cells. **F,** Time-course OCR assay in tumor cell lines with genetic deletion of RIP1 or RIP3 versus wild-type cells showing the effects of CM272 treatment at IC_{50} dose. **G,** Schematic representation of the TCA cycle including metabolites, enzymes, and substrates. **H,** Measurement of PDH complex and GLUD1 enzymatic activities and glutamate incorporation in K422 and HBL1 cells after treatment with CM272 and vorinostat. **I,** LC/MS analysis using ^{13}C-labeled glucose or glutamine in HBL1 cells treated with CM272 during 24 hours at IC_{25} and IC_{50} doses in comparison with untreated cells. **J,** Relative abundance of TCA cycle metabolites in HBL1 cells treated with CM272 during 24 hours at IC_{25} and IC_{50} doses in comparison with untreated cells (left). Relative abundance of succinate with respect to other TCA cycle metabolites in K422 and HBL1 cells treated with CM272 during 24 hours at IC_{25} and IC_{50} doses in comparison with untreated cells (right). *, $P < 0.05$; **, $P < 0.01$; ***, $P < 0.001$.

by LC/MS using ^{13}C-labeled glucose or ^{13}C-labeled glutamine. Epigenetic drugs increased the abundance of citrate, glutamate, fumarate, malate, and aspartate, which were predominantly produced by both labeled glucose and glutamine (Fig. 4I; Supplementary Fig. S4G). In contrast, the relative abundance of succinate with respect to other TCA cycle metabolites decreased dramatically following drug exposure (Fig. 4I and J). Additional LC/MS studies revealed higher quantities of ^{13}C-non-labeled amino acids (alanine, glycine, leucine, isoleucine, serine, and tryptophan) after epigenetic therapy, indicating an increase in their uptake from the culture media to further fuel the TCA cycle (Supplementary Fig. S4H). In conclusion, epigenetic drugs globally enhance the function of the TCA cycle by incorporating glucose and glutamine, which are the two major energy substrates of cancer cells (33), but this paradoxically results in a marked depletion of succinate.

Hyperfunctional Succinate Dehydrogenase Generates Excessive Reactive Oxygen Species and Triggers Tumor Necroptosis

Succinate reduction could reflect its high consumption as a substrate fueling the enzymatic complex II in electron transport chain (ETC) to generate mitochondrial ATP. To investigate this possibility, functional examination of ETC complexes was next performed (Fig. 5A). Following epigenetic treatment, high enzymatic activity of succinate dehydrogenase (SDH) in ETC complex II was observed, whereas activities of complexes I (NADH dehydrogenase), III (cytochrome c reductase), IV (cytochrome c oxidase), and V (ATP synthase complex) remained constant (Fig. 5B). The enzymatic activity of SDH, however, was not affected in RIP1-deficient cells (Fig. 5C; Supplementary Fig. S5A). SDH catalyzes electron transfer from succinate to the electron carrier, but electrons can leak out to molecular oxygen to form reactive oxygen species (ROS; ref. 34). Accordingly, dose-dependent increases in mitochondrial ROS levels were observed after epigenetic therapies, which were not observed in cells with deletion of RIP1 (Fig. 5D and E; Supplementary Fig. S5B). To determine whether tumor cell death was caused by the cell's inefficiency to compensate ATP depletion, by excessive ROS, or by both, the effects of epigenetic drugs in combination with the pharmacologic inhibition of SDH in complex II (which generates ROS) and of ATP synthase in complex V (which generates ATP) were compared (35). Targeting of SDH consistently decreased the antitumor effect of epigenetic therapies, whereas inhibition of ATP synthase did not (Fig. 5F; Supplementary Fig. S5C). Thus, increased SDH function triggers excessive mitochondrial ROS that promotes tumor cell death. In line with this notion, inhibition of complexes I and III (which also participate in ROS generation), but not of complex IV (which collaborates to synthesize ATP), consistently decreased the antitumor effects of epigenetic therapies (Supplementary Fig. S5D). Accordingly, addition of several ROS inhibitors markedly decreased the antitumor effect of epigenetic drugs (Fig. 5G; Supplementary Fig. S5E). Moreover, blocking the use of glucose or glutamine in the TCA cycle by pharmacologic inhibition of PDH or GLUD1 functions, respectively, decreased tumor cell death rates after drug exposure (Fig. 5H; Supplementary Fig. S5F). Furthermore, fueling the TCA cycle with nonessential amino acids including glutamine potentiated the effects of epigenetic agents, whereas glutamine deprivation induced the opposite effects (Supplementary Fig. S5G). Finally, we took advantage of the loss-of-function mutations in mitochondrial complex I genes recurrently found in cancer cells, which impair mitochondria respiration and thereby limit ROS generation (36). As expected, tumors with complex I mutations exhibited worse tolerance to glucose deprivation, while being insensitive to glutamine restriction (Supplementary Fig. S5H). Remarkably, tumor cell lines with complex I mutations were more resistant to epigenetic therapies than nonmutated tumors, which points to OXPHOS dynamics as a potential biomarker of response to the drugs (Fig. 5I). These results show that epigenetic drugs induce cancer cell death by promoting excessive oxidative stress in mitochondria.

Epigenetic Agents and BH3 Mimetics Exhibit Synergistic Effects in Multiple Tumor Types

Based on these findings, we postulated that the drug-induced deregulation of mitochondrial metabolism might be priming cells to mitochondrial apoptosis. To investigate this hypothesis, AML cell lines were incubated with DNMT, HDAC, or HMT drug inhibitors and the BCL2 inhibitor venetoclax (which specifically induces mitochondrial apoptosis), which in combination triggered potent synergistic effects (Fig. 6A; Supplementary Table S2A). Evaluation of this combination therapy was next performed in other tumor types. Epigenetic drugs and venetoclax were also synergistically active in B-cell leukemia and lymphoma cell lines *in vitro* and *in vivo* (Fig. 6B and C; Supplementary Table S2B). However, a minority of AML and lymphoma cell lines (6 of 36, 17%) did not respond to the combination therapy (Fig. 6A and B). Such refractoriness was explained because the six tumors lacked or showed minor BCL2 expression and therefore were resistant to venetoclax (Supplementary Fig. S6). However, the

Figure 5. Hyperfunctional SDH induces excessive oxidative stress that triggers tumor cell necroptosis. **A,** Schematic representation of mitochondrial ETC complexes and the generation of ATP and ROS. **B,** Quantification of the enzymatic activities of ETC complexes I to V in K422 and HBL1 cells treated with CM272 or vorinostat at IC_{50} doses during 24 hours. **C,** Effects of CM272 on the enzymatic activity of ETC complex II in wild-type (WT) and RIP1-deficient HAP1 and HT29 cells. **D,** Measurement of mitochondrial ROS levels in K422 and HBL1 cells treated with CM272 and vorinostat during 24 hours at IC_{25} and IC_{50} doses. **E,** Levels of mitochondrial ROS in wild-type and RIP1-deficient HAP1 and HT29 cells. **F,** Cell viability of K422 and HBL1 cells upon pharmacologic inhibition of complex II with dimethyl-malonate and of complex V with oligomycin, in combination with CM272 at IC_{50} doses (left). The reduction of tumor cell death with complex II inhibition is not observed in HAP1 and HT29 cells with genetic ablation of RIP1. **G,** Cell viability of tumor K422 and HBL1 cells after treatment with CM272 alone and combined with the ROS inhibitors N-acetyl cysteine (NAC), glutathione (GSH), mitoTEMPO, butylated hydroxyanisole (BHA), and ascorbic acid (left). Reduction of tumor cell death is not observed in HAP1 and HT29 cells with RIP1 deletion in comparison with wild-type cells (right). **H,** Effects on cell viability of the pharmacologic inhibition of PDH function with two different compounds, CPI-613 and 3-BrPA/4BPM, and of the inhibition of GLUD1 function with the R162 inhibitor in K422 and HBL1 cells treated with CM272. The changes in cell viability are not observed in HAP1 cells with deletion of RIP1. **I,** Representative curves of cell viability in tumor cell lines from hematologic malignancies treated with CM272 or vorinostat at increasing doses during 24 hours. Tumors with complex I mutations are U937 and SUDHL16, and tumors without complex I mutations include MV411, DOHH2, and OCIAML2 (according to ref. 36). *, $P < 0.05$; **, $P < 0.01$; ***, $P < 0.001$. n.s. values are not shown.

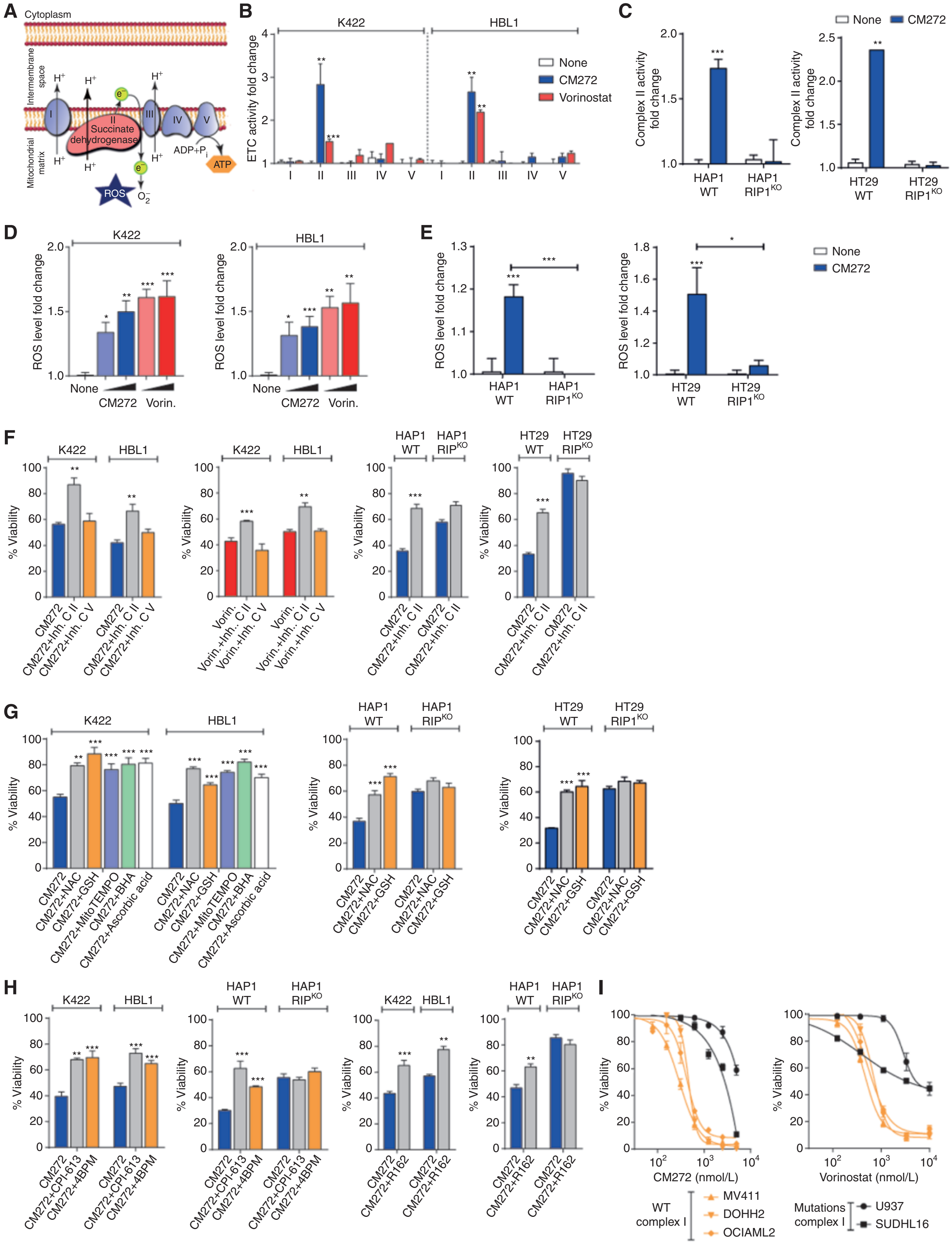
A
Cytoplasm
Intermembrane space
Mitochondrial matrix
H+
e−
I
II Succinate dehydrogenase
III
IV
V
ADP+Pi
ATP
ROS
O2−
B
K422
HBL1
ETC activity fold change
None
CM272
Vorinostat
I II III IV V I II III IV V
C
Complex II activity fold change
HAP1 WT
HAP1 RIP1KO
HT29 WT
HT29 RIP1KO
None
CM272
D
ROS level fold change
None
CM272
Vorin.
E
ROS level fold change
HAP1 WT
HAP1 RIP1KO
HT29 WT
HT29 RIP1KO
None
CM272
F
% Viability
CM272
CM272+Inh. C II
CM272+Inh. C V
Vorin.
Vorin.+Inh. C II
Vorin.+Inh. C V
HAP1 WT
HAP1 RIPKO
HT29 WT
HT29 RIPKO
G
% Viability
CM272
CM272+NAC
CM272+GSH
CM272+MitoTEMPO
CM272+BHA
CM272+Ascorbic acid
H
% Viability
CM272
CM272+CPI-613
CM272+4BPM
CM272+R162
I
% Viability
CM272 (nmol/L)
Vorinostat (nmol/L)
WT complex I
MV411
DOHH2
OCIAML2
Mutations complex I
U937
SUDHL16

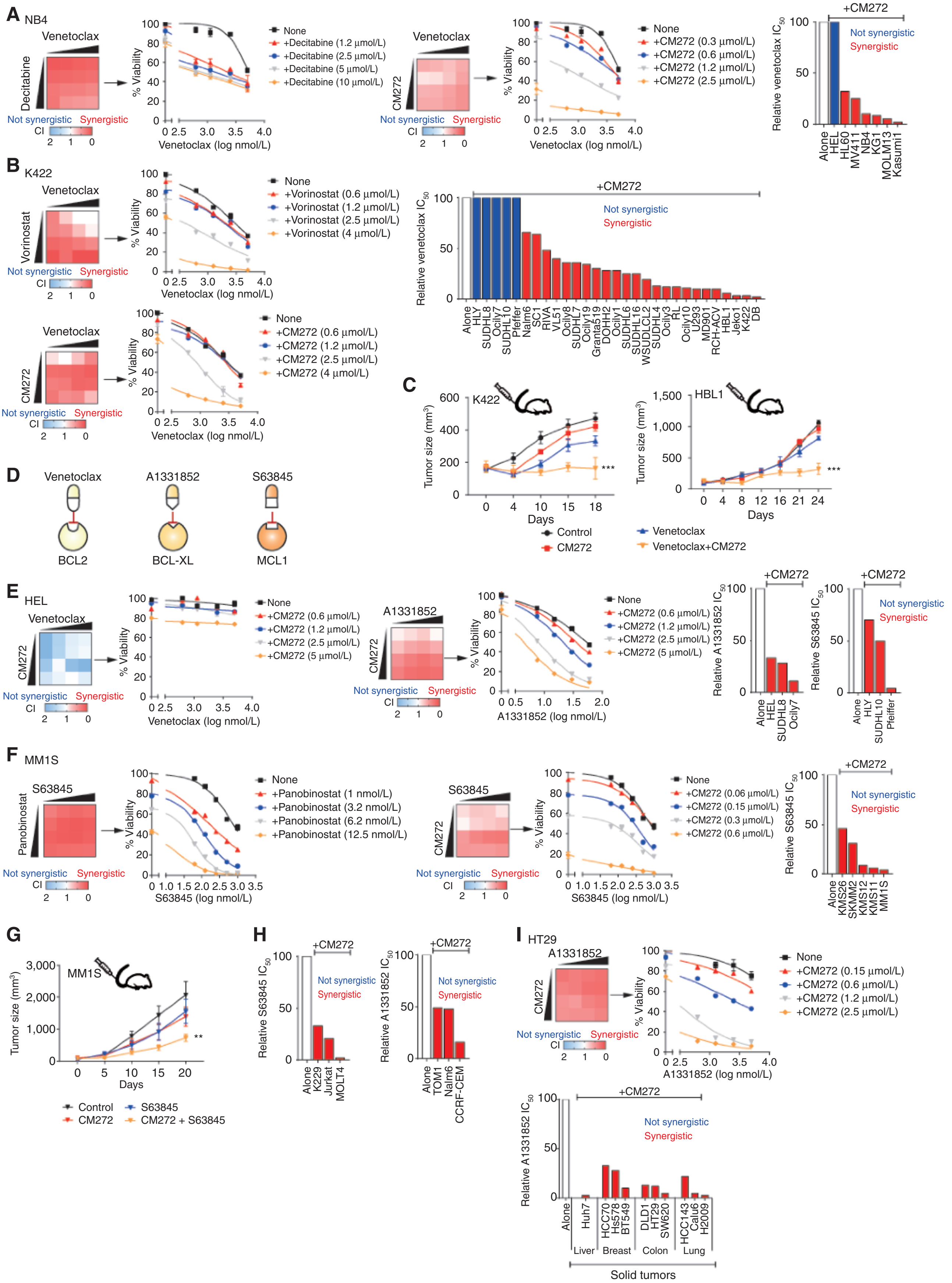
A NB4
Venetoclax
Decitabine
Not synergistic Synergistic
CI 2 1 0
% Viability
Venetoclax (log nmol/L)
None
+Decitabine (1.2 µmol/L)
+Decitabine (2.5 µmol/L)
+Decitabine (5 µmol/L)
+Decitabine (10 µmol/L)
CM272
+CM272 (0.3 µmol/L)
+CM272 (0.6 µmol/L)
+CM272 (1.2 µmol/L)
+CM272 (2.5 µmol/L)
Relative venetoclax IC50
+CM272
Alone HEL HL60 MV411 NB4 KG1 MOLM13 Kasumi1
B K422
Vorinostat
+Vorinostat (0.6 µmol/L)
+Vorinostat (1.2 µmol/L)
+Vorinostat (2.5 µmol/L)
+Vorinostat (4 µmol/L)
+CM272 (0.6 µmol/L)
+CM272 (1.2 µmol/L)
+CM272 (2.5 µmol/L)
+CM272 (4 µmol/L)
Alone HLY SUDHL8 Ocily7 SUDHL10 Pfeffer Nalm6 SC1 RIVA VL51 Ocily8 SUDHL7 Ocily19 Granta519 DOHH2 Ocily1 SUDHL6 SUDHL16 WSUDLCL2 SUDHL4 Ocily3 RL Ocily10 U293 MD901 RCH-ACV HBL1 Jeko1 K422 DB
C K422 HBL1
Tumor size (mm3)
Days
***
Control
CM272
Venetoclax
Venetoclax+CM272
D Venetoclax A1331852 S63845
BCL2 BCL-XL MCL1
E HEL
+CM272 (0.6 µmol/L)
+CM272 (1.2 µmol/L)
+CM272 (2.5 µmol/L)
+CM272 (5 µmol/L)
A1331852
A1331852 (log nmol/L)
Relative A1331852 IC50
Alone HEL SUDHL8 Ocily7
Relative S63845 IC50
Alone HLY SUDHL10 Pfeiffer
F MM1S
S63845
Panobinostat
+Panobinostat (1 nmol/L)
+Panobinostat (3.2 nmol/L)
+Panobinostat (6.2 nmol/L)
+Panobinostat (12.5 nmol/L)
S63845 (log nmol/L)
+CM272 (0.06 µmol/L)
+CM272 (0.15 µmol/L)
+CM272 (0.3 µmol/L)
+CM272 (0.6 µmol/L)
Alone KMS26 SKMM2 KMS12 KMS11 MM1S
G MM1S
**
Control S63845
CM272 CM272 + S63845
H
Alone K229 Jurkat MOLT4
Alone TOM1 Nalm6 CCRF-CEM
I HT29
+CM272 (0.15 µmol/L)
+CM272 (0.6 µmol/L)
+CM272 (1.2 µmol/L)
+CM272 (2.5 µmol/L)
Alone Huh7 HCC70 Hs578 BT549 DLD1 HT29 SW620 HCC143 Calu6 H2009
Liver Breast Colon Lung
Solid tumors

resistant tumors expressed MCL1 and/or BCL-XL proteins, which together with BCL2 constitute the key antiapoptotic members of the intrinsic mitochondrial pathway (Fig. 6D; ref. 22). Accordingly, BH3-mimetic drugs targeting MCL1 or BCL-XL in combination with epigenetic therapies recapitulated the synergistic responses in venetoclax-resistant cell lines (Fig. 6E; ref. 37). AML and B-cell malignancies are preferentially BCL2-dependent tumors (22), whereas multiple myeloma depends on MCL1 for survival (38). Therefore, in this hematologic malignancy, we tested epigenetic drugs in combination with an MCL1 inhibitor. In *in vitro* and *in vivo* experiments, multiple myeloma cells synergistically responded to these combinations (Fig. 6F and G; Supplementary Table S2C). In addition, T-cell leukemia and lymphoma cell lines synergistically responded to either MCL1 or BCL-XL inhibition combined with epigenetic therapies, confirming the dual dependence for survival on MCL1 and BCL-XL of T-cell malignancies (Fig. 6H; Supplementary Table S2D; ref. 39). Moreover, lung, breast, colon, and liver cancer–derived cell lines synergistically responded to epigenetic therapies with selective BCL-XL inhibition, indicating the role of this antiapoptotic protein in solid tumors (Fig. 6I and Supplementary Table S2E; ref. 40). Taken together, DNMT, HDAC, and HMT inhibitors and proapoptotic agents induce synergistic responses in cell lines from multiple hematologic malignancies and solid tumors, given that the appropriate BH3-mimetic drug is used on each particular tumor. These findings could provide a mechanistic rationale to the results of AML clinical trials, which showed potent synergistic responses to the combination of DNMT inhibitors and venetoclax and significantly extended patient survival (41, 42)

Mechanistic Basis of the Synergistic Therapy

To further investigate the mechanism by which hyperactive OXPHOS deregulated mitochondria and broadly sensitized tumor cells to proapoptotic molecules, changes in mitochondrial transmembrane potential ($\Delta\Psi_{\mathrm{mito}}$) were next measured by tetramethylrhodamine ethyl ester (TMRE) fluorescence. Time-course TMRE assays revealed that epigenetic drugs rapidly increased $\Delta\Psi_{\mathrm{mito}}$, which reflects hyperpolarization of the mitochondrial membrane caused by accumulation of protons in exchange by electrons (Fig. 7A; see Fig. 5A). However, caspase activation was not observed, indicating that the hyperpolarized membrane remained intact and restrained intrinsic apoptosis during therapy (Fig. 7B). In contrast, adding venetoclax to epigenetic drug therapy abruptly depolarized mitochondria membrane (shown by the marked drop of $\Delta\Psi_{\mathrm{mito}}$ values) and induced caspase cleavage, indicative of collapsed mitochondria leading to caspase-mediated apoptosis (Fig. 7A and B). In this context, pharmacologic inhibition of SDH function in the ETC complex II reduced the mitochondria hyperpolarization that was triggered by epigenetic agents, resulting in the attenuation of their antitumor effects in combination with venetoclax (Fig. 7C). These results highlight the role of SDH activity to increase mitochondria hyperpolarization and block apoptosis, which modulates the therapeutic synergy. To investigate how the blockade of mitochondrial apoptosis occurs and sensitizes to the effects of venetoclax, Western blot and gene expression analyses of BCL2 family members and of other components of the intrinsic and extrinsic apoptotic pathways were performed before and after treatment. Although consistent expression changes were not observed, cotranslocation of antiapoptotic BCL2 and proapoptotic BAX proteins from cytosol to mitochondria was detected after epigenetic therapy (Fig. 7D; Supplementary Fig. S7A). Thus, BCL2 sequestrates BAX in the hyperpolarized mitochondria, thereby blocking its effector proapoptotic function during epigenetic therapy. Accordingly, BCL2 inhibition with venetoclax releases BAX effector activity that unleashes caspase-mediated apoptosis in tumor cells. Consequently, the combination of epigenetic drugs and BH3 mimetics induced both RIP1-mediated necroptosis and caspase-mediated apoptosis (Fig. 7B). Moreover, electron microscopy showed unique ultrastructural features of simultaneous necroptosis and apoptosis in tumor cells treated with the combination therapy (Fig. 7E). Corroborating these findings, necrostatin and z-VAD administered together totally reversed the synergistic responses (Fig. 7F; Supplementary Fig. S7B–S7D). Therefore, hyperactive mitochondria block apoptosis by increasing BCL2 dependency in order to maintain ATP generation, which leads to tumor necroptosis and sensitizes to mitochondrial apoptosis.

Therapeutic Synergy in Primary Cells from Multiple Cancers

Finally, the combination therapy was tested in primary samples from patients with cancer. In lymphoid and myeloid malignancies, epigenetic drugs induced ERV-mediated

Figure 6. Synergistic responses to epigenetic agents and BH3-mimetics in multiple cancer types. **A,** Representation of the combination index (CI) values and cell viability curves of venetoclax with decitabine (left) or CM272 (middle) at increasing concentration in AML cells. Synergistic effect between two drugs was defined for values of CI < 1 in at least four drug–drug interactions. On the right, reduction of venetoclax IC_{50} values for its combination with CM272 is depicted in 6 AML-derived cell lines. Tumors showing synergistic effect are colored in red, whereas those without synergism are colored in blue. **B,** CI values and cell viability curves of venetoclax with vorinostat or CM272 in B-cell lymphoma and leukemia cells. On the right, reduction of venetoclax IC_{50} values for its combination with CM272 in 29 B-cell lymphoma cell lines. **C,** *In vivo* therapy trial of CM272 and venetoclax in two tumor xenograft cell line models (K422 and HBL1). 5×10^6 cells were injected s.c. into immunodeficient Rag2$^{-/-}$IL2γc$^{-/-}$ 8-week-old female mice, which were untreated (control), treated with CM272 (2.5 mg/kg), with venetoclax (50 mg/kg), and with CM272 and venetoclax. Treatment was administrated i.p. for 5 consecutive days per week during 2 weeks. At least 8 mice were included per treatment cohort. **D,** Representation of BCL2, MCL1, and BCL-XL antiapoptotic proteins and their corresponding drug inhibitors. **E,** Venetoclax-resistant DLBCL ($n = 5$) and AML ($n = 1$) cell models synergistically respond to the combination of epigenetic agents with MCL1 or BCL-XL inhibitors. On the left, synergistic effects were observed in HEL cells treated with the BCL-XL inhibitor A1331852 but not with venetoclax. On the right, reduction of A1331852 or S63485 IC_{50} values for their combination with CM272 in the six venetoclax-resistant tumors. **F,** Synergistic effects of panobinostat or CM272 with the MCL1 inhibitor S63845 in multiple myeloma cell lines. **G,** *In vivo* combination therapy of multiple myeloma MM1S cell line. 5×10^6 cells were injected s.c. into Rag2$^{-/-}$IL2γc$^{-/-}$ 8-week-old female mice, which were untreated (control), treated with CM272 (2.5 mg/kg), with S63845 (50 mg/kg), and with CM272 and S63845. Treatment was administrated i.p. for 5 consecutive days per week during 2 weeks. At least 8 mice were included per treatment cohort. **H,** Synergistic effect of CM272 with BCL-XL or MCL1 inhibition therapy in T-cell acute lymphoblastic leukemia cell lines. **I,** Synergistic effect of CM-272 with BCL-XL and MCL1 inhibition in lung, breast, liver, and colon cancer cell line models. **, $P < 0.01$; ***, $P < 0.001$.

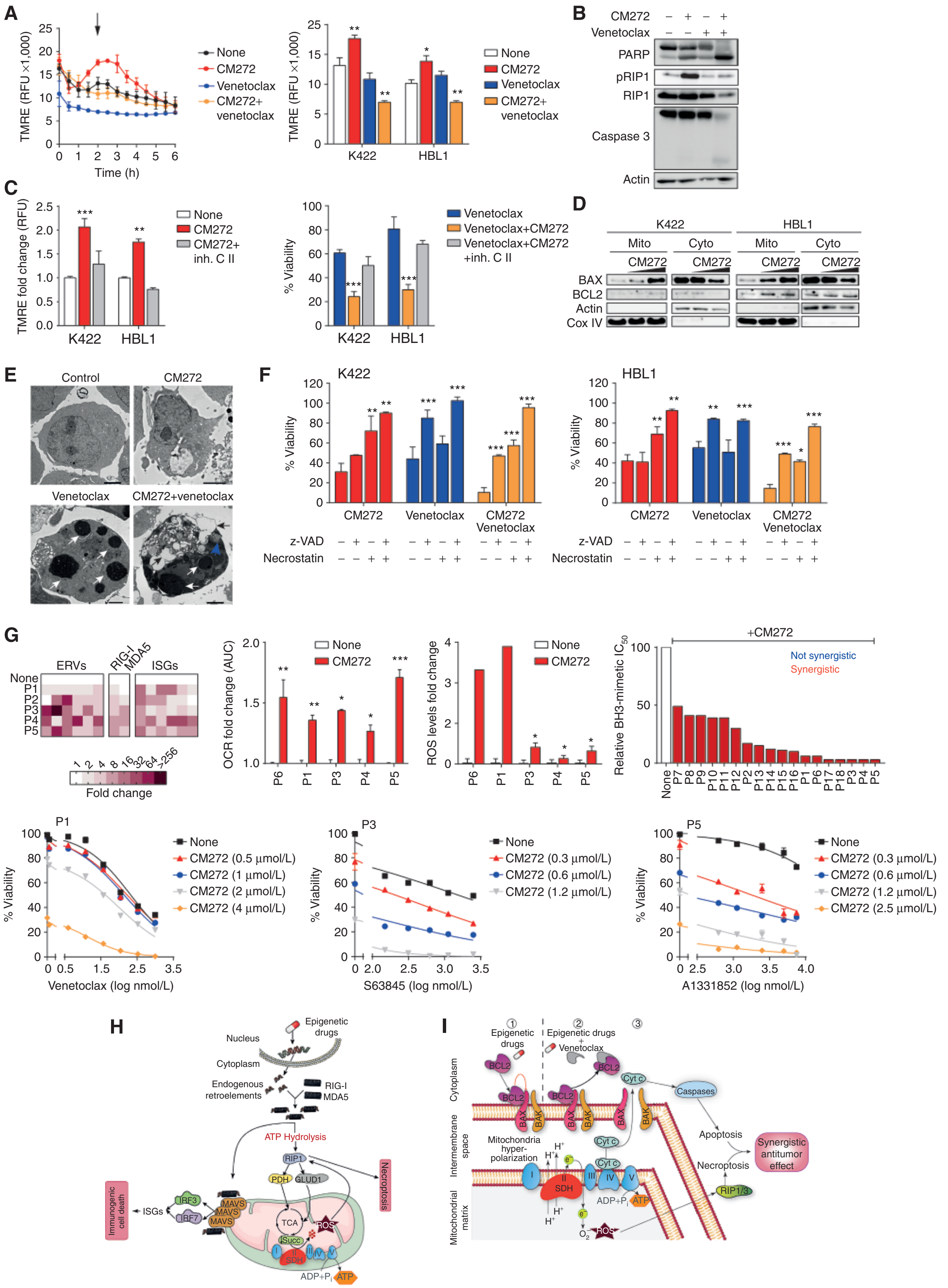
A
TMRE (RFU ×1,000)
Time (h)
None
CM272
Venetoclax
CM272+ venetoclax
K422
HBL1
B
CM272
Venetoclax
PARP
pRIP1
RIP1
Caspase 3
Actin
C
TMRE fold change (RFU)
None
CM272
CM272+ inh. C II
% Viability
Venetoclax
Venetoclax+CM272
Venetoclax+CM272 +inh. C II
D
K422
HBL1
Mito
Cyto
BAX
BCL2
Actin
Cox IV
E
Control
CM272
Venetoclax
CM272+venetoclax
F
z-VAD
Necrostatin
G
ERVs
RIG-I MDA5
ISGs
None
P1
P2
P3
P4
P5
Fold change
OCR fold change (AUC)
P6
ROS levels fold change
Relative BH3-mimetic IC50
+CM272
Not synergistic
Synergistic
P1
P3
P5
CM272 (0.5 μmol/L)
CM272 (1 μmol/L)
CM272 (2 μmol/L)
CM272 (4 μmol/L)
CM272 (0.3 μmol/L)
CM272 (0.6 μmol/L)
CM272 (1.2 μmol/L)
CM272 (2.5 μmol/L)
Venetoclax (log nmol/L)
S63845 (log nmol/L)
A1331852 (log nmol/L)
H
Epigenetic drugs
Nucleus
Cytoplasm
Endogenous retroelements
RIG-I
MDA5
ATP Hydrolysis
RIP1
PDH
GLUD1
TCA
Succ
ROS
SDH
ADP+Pi
ATP
Necroptosis
Immunogenic cell death
ISGs
IRF3
IRF7
MAVS
I
① Epigenetic drugs
② Epigenetic drugs + Venetoclax
③
Cytoplasm
Intermembrane space
Mitochondrial matrix
BCL2
BAX
BAK
Cyt c
Caspases
Apoptosis
Necroptosis
Synergistic antitumor effect
Mitochondria hyper-polarization
RIP1/3
H+
e−
O2
ROS

responses, increased OCR and ROS levels, and sensitized tumor cells to BCL2 and/or MCL1 targeting (Fig. 7G; Supplementary Table S3). Likewise, in xenografts derived from patients with lung cancer treated with epigenetic therapies, antiviral responses led to increased OCR and ROS levels that yielded synergistic responses with BCL-XL inhibitors (Fig. 7G). Therefore, as in patient-derived cell lines, epigenetic therapies show synergistic effects in combination with BH3 mimetics in primary patient samples.

DISCUSSION

Here, we decipher a mechanistic model by which epigenetic drug inhibitors kill cancer cells through deregulating energy metabolism (Fig. 7H). This effect does not contradict the antitumor activities of the different epigenetic drugs driven by selective enzymatic inhibition, by epigenetically mediated reactivation of tumor-suppressor genes, or by increased tumor immunogenicity leading to immune-related cell death. Rather, our data reveal a common antitumor mechanism upon targeting of heterochromatic structures that transcriptionally repress endogenous retroelements, including ERVs and long and short interspersed nuclear elements (LINEs and SINEs, respectively), which once reexpressed cause profound metabolic changes leading to tumor cell death (6, 8, 43). A recent study showed that intronic and intergenic SINEs, specifically Alu retroelements, are the major source of immunogenic responses mediated by MDA5 sensor in tumor cells upon epigenetic therapy (44). Whether SINEs are also more capable among the different retroelements to deplete intracellular ATP and rewire tumor energetic metabolism remains to be explored. Our data suggest that the common metabolic deregulation upon retroelement activation underlies the broad responses to epigenetic therapies in cancers with different phenotypic, genotypic, and epigenetic features.

The discovery of energy metabolism as a determinant element of the antitumor effect of epigenetic therapies may explain their preference to eliminate cancer cells while sparing most nontumor cells. Thus, tumors are “addicted” to the Warburg effect through oncogenic mutations that constitutively promote cell proliferation and increase bioenergetic demands, thereby becoming more susceptible to the metabolic crisis induced by epigenetic therapies. In contrast, normal proliferating cells can undergo quiescence and limit metabolic requirements under energetic restrictions, therefore better tolerating the metabolic effects of epigenetic drugs (29, 33, 45, 46). Our findings could also underpin the higher activity of the drugs in hematologic malignancies in comparison with solid tumors, because highly proliferative lymphoid and myeloid neoplasms are more addicted to the Warburg effect, being primarily sustained by glycolysis and exhibiting poor tolerance to OXPHOS metabolism, whereas most solid tumors are less proliferative and tend to use OXPHOS more commonly (29, 33, 45, 46). Undoubtedly, the deregulation of energy metabolism by targeting the epigenome opens new research avenues with immediate scientific and clinical consequences, particularly in combination therapies.

Thus, we disclose here an intimate mechanism by which DNMT, HDAC, and HMT inhibitors and BH3-mimetic drugs are synergistically active in multiple tumor types (Fig. 7I). Beyond a previous study defining the effect of hypomethylating agents in combination with venetoclax on leukemic stem cells (41), our results provide a broader mechanistic basis that may underlie the extraordinary results of clinical trials in patients with AML (42). Based on our findings, we suggest the development of similar clinical trials in patients with other hematologic malignancies with poor prognosis, preferentially those where epigenetic drugs and venetoclax are in clinical practice (37, 47–49). Similar drug combinations could also be tested in patients with advanced, metastatic, and refractory solid tumors, on the basis of the promising responses to these drugs in preclinical studies and/or early clinical trials (50). Finally, because epigenetic agents prime tumor cells to the effects of immune checkpoint inhibitors through cell-extrinsic mechanisms (13, 14), and we show here that the drugs sensitize tumors to proapoptotic molecules at the cell-intrinsic level, we envisage that a triple combination of epigenetic agents, PD-1/PD-L1 inhibitors, and BH3 mimetic will induce potent and durable responses in currently incurable cancers.

METHODS

Tumor Cell Lines

Tumor cell lines are listed in the Resources Table as Supplementary Material. If not indicated otherwise, cell lines were maintained in RPMI-1640 medium, 10% (v/v) FBS, 2% P/S (penicillin 100 U/mL and streptomycin 0.1 mg/mL), glutamine (2 mmol/L), and HEPES (25 mmol/L) at 37°C in a humid atmosphere containing 5% CO_2 with few exceptions. OCILY1, OCILY7, and HAP1 cells were cultured in Iscove’s Modified Dulbecco’s Medium (IMDM). OCILY3 cells and

Figure 7. Mechanistic basis of the synergistic combination therapy. **A,** Time-course TMRE fluorescence measurement revealed an increase in $\Delta\Psi_{mito}$ following epigenetic therapy, which markedly drops with the addition of venetoclax. CM272 and venetoclax were used at IC_{25} dose, alone and in combination. On the right, TMRE fluorescence quantification in tumor cells after 2 hours of treatment (marked with an arrow). **B,** Western blot analyses of PARP cleavage, RIP1 phosphorylation, and caspase 3 cleavage and in tumor cells treated with epigenetic drugs and venetoclax alone and in combination. Cells were treated during 24 hours with CM272 at IC_{25} dose and/or venetoclax at IC_{25}. **C,** TMRE decrease after inhibition of SDH enzymatic activity with dimethyl-malonate (left), which leads to a decrease of the synergistic effects of epigenetic drugs combined with venetoclax (right). Cells were treated during 24 hours with CM272 at IC_{50} dose. **D,** Western blot analysis of BCL2 and BAX in mitochondria and cytosol protein fractions in untreated cells and in cells treated with increasing doses of CM272 (IC_{25} and IC_{50}). **E,** Electron microscopy of tumor-treated cells showing features of simultaneous necroptosis and apoptosis. Cells were treated during 24 hours with CM272 at IC_{50} dose and/or venetoclax at IC_{50} dose. Morphologic signs of necroptosis, including cell membrane rupture, cytoplasm vacuolization, and swelled mitochondria, are marked with black arrows, whereas typical signs of apoptosis, including pyknotic and shrunken nuclei with condensed cytoplasm, are marked with white arrows. **F,** Necrostatin and z-VAD completely reversed the effects of CM-272 and venetoclax combination. Cells were treated during 24 hours with CM272 at IC_{50} dose and/or venetoclax at IC_{50}. **G,** Primary samples from hematologic malignancies and solid tumors incubated with CM272 and proapoptotic inhibitors. Measurement of the expression of ERVs, RIG-I and MDA5 coding genes, and ISGs was performed using qRT-PCR after 24 hours of treatment. OCR quantification and measurement of ROS levels were performed in tumor cells after 24 hours of treatment. Cell viability curves were calculated as in Fig. 6. **H,** Schematic representation of the antitumor action of epigenetic drugs in cancer by activating endogenous retroelements. **I,** Schematic representation of the mechanisms underlying the synergistic effect of epigenetic drugs and BH3-mimetics in cancer. *, $P < 0.05$; **, $P < 0.01$; ***, $P < 0.001$. n.s. values are not shown.

patient-derived xenografts were cultured in IMDM with 20% FBS. OCILY10 cells were cultured in IMDM containing 20% human serum. HuH7 cells deficient for RIG-I and MAVS, and HT29 and L929 cells with genetic ablation of RIP1, RIP3, and MLKL were reported previously (32, 51, 52). All cell lines were tested negative for *Mycoplasma*.

Generation of HAP1 Knock-Out Cell Lines by CRISPR/Cas9 Technology

HAP1 cells are a near-haploid cell line derived from the KBM-7 cell line, which was derived from a patient with chronic myeloid leukemia in transformation to AML (blast phase). HAP1 knock-out (KO) cell lines (Horizon Discovery) were engineered using CRISPR/Cas9 to delete a variable number of base pairs causing a frameshift in the corresponding gene. MAVS KO cells were generated using CCTGGGGGTG GAACGGGCCA as guide RNA and included a 4 bp deletion in exon 6; RIG-I KO cells were generated using AAACAACAAGGGCCCAATGG as guide RNA and included a 11 bp deletion in exon 2; MDA5 KO cells were generated using TTGGACTCGGGAATTCGTGG as guide RNA and included a 13 bp deletion in exon 1; double RIG-I/MDA5 KO cells were generated using TTGGACTCGGGAATTCGTGG as guide RNA for MDA5 in RIG-I KO cells; IRF3 KO cells were generated using AGGGCTCAGGGGCTACAGCC as guide RNA and included a 40 bp in exon 5; IRF7 KO cells were generated using CTTCCAGGGCACGCG GAAAC as guide RNA and included a 13 bp deletion in exon 1; and RIPK1 KO cells were generated using AGTACTCCGCTTTCTGTAAA as guide RNA and included 14 bp in exon 3. Genomic deletions were confirmed by PCR on genomic DNA and by Western blot using appropriate antibodies.

Primary Patient Samples

Human tumor samples were obtained from the University of Navarra Biobank, all of which included an informed written consent obtained from the subjects. Peripheral blood or bone marrow mononuclear cells from patients with hematologic malignancies were separated by Ficoll density gradient centrifugation (Ficoll-Paque Plus; GE Healthcare) and incubated in IMDM supplemented with 20% FBS and 2% P/S. AML cells were cultured and expanded in the Stemspan leukemic cell culture medium. Tumor-derived xenografts from patients with lung cancer were obtained from primary effusions and equally processed. All studies were conducted with appropriate institutional University of Navarra Ethics Committee approval.

Cell Viability and Cell Death Assays

Cells were seeded in 96-well culture plates at a density of 2 to 3×10^4 cells/well and treated with the different epigenetic or proapoptotic drugs alone or in combination for 24 to 48 hours. Cell viability was quantified using MTS (Promega). Cell death was measured using the Annexin V–FITC Apoptosis Detection Kit (BD Biosciences), according to the manufacturer's instructions, and analyzed in a FACSCantoII (BD Biosciences). All experiments were performed in triplicate.

Quantitative Real-Time PCR

Total RNA was isolated using Tri reagent (Sigma-Aldrich) followed by DNase I (Thermo Fisher Scientific) treatment to avoid the effect of DNA contamination. cDNA was synthesized using random primers and M-MLV reverse transcriptase enzyme (Invitrogen) according to the manufacturer's protocol. Relative gene expression was determined by qRT-PCR with gene-specific primers and SYBR Select Master Mix (Applied Biosystems) on a -ViiA 7 Real-Time PCR system (Applied Biosystems). Gene expression was analyzed by the 2-ΔΔCt method by normalizing the expression of each gene to PGK1 and then to the control. Primers for qRT-PCR are listed in Supplementary Table S1. All experiments were performed in triplicate.

Immunofluorescence Analysis and Confocal Microscopy

Immunofluorescence was performed as previously reported (53). Briefly, after 24 hours of treatment, tumor cells were harvested, washed once with PBS, and fixed with 4% formaldehyde (Thermo Fisher Scientific) for 10 minutes and washed 3 times for 5 minutes with PBS. Cell permeabilization and blocking were performed using PBS, 0.5% Triton-X-100 for 15 minutes and PBS, 0.25% BSA for 1 hour, respectively. Subsequently, the primary antibody for dsRNAs (clone J2), RIG-I, or MDA5 was added and incubated overnight at 4°C. The following day, cells were washed 3 times for 5 minutes with PBS and incubated with the secondary antibody for 1 hour at room temperature. After three washes for 5 minutes with PBS, cells were mounted on a slide with prolong glass antifade mountant containing DAPI staining (Thermo Fisher Scientific). Images were acquired using a Confocal Scanning Laser Microscopy Zeiss LSM 800, and pictures were then analyzed using the ZEN 2 (Zeiss) software. No unspecific staining was observed with the secondary antibody used.

Western Blotting and Semi-Denaturing Detergent Agarose Gel Electrophoresis

Western blot analyses were performed following reported methods (54). Briefly, tumor cells (6×10^5 cells/mL) were treated with the corresponding drug for 24 hours; then washed twice with PBS and lysed in buffer A [50 mmol/L HEPES, pH 7.5; 150 mmol/L NaCl; 2.5 mmol/L EDTA; and 1% (v/v) Triton X-100] containing 30 mmol/L NEM, 1 mmol/L PMSF, and 1 x Complete Protease Inhibitor (Roche); and centrifuged at 6,000 rpm for 10 minutes at 4°C. Soluble proteins were quantified using BCA protein assay kit, and concentrations were adjusted in sample buffer [2X TBE, 20% (v/v) glycerol, and 4% (w/v) SDS, Bromophenol blue]. Protein samples were incubated for 15 minutes at room temperature before loading on a 1.8% agarose gel. Electrophoresis was performed in running buffer (1× TBE and 0.1% SDS) with a constant voltage of 50 V at room temperature, and then proteins were transferred to nitrocellulose membrane. Western blot bands were quantified using ImageJ software. Antibodies are listed in the Resources Table in the Supplementary Material.

Glucose Quantification, Lactate Extrusion, and ADP/ATP Ratio Measurements

Glucose and lactate levels were quantified by using the glucose HK CP ABX PENTRA kit and the Lactic Acid ABX Pentra kit, respectively, according to the manufacturer's instructions. Results were normalized to total protein content of cell extracts. ADP and ATP levels were quantified using the ADP/ATP Ratio Assay Kit in cultured cells treated with different concentrations of the drugs for 24 hours. Luminescence was measured using the Lumat LB 9507 (Berthold Technologies). The ADP/ATP ratio was calculated according to the manufacturer's protocol. Glycolytic and mitochondrial ATP production was measured in an XF24 Extracellular flux analyzer (Seahorse Biosciences), according to the manufacturer's instructions.

Glucose Oxidation Measurement

After CM272 treatment during 24 hours, cells in 6-well plates were incubated during 2 hours in 1 mL Krebs Ringer buffer containing 2% BSA, 10 mmol/L HEPES, 2 mmol/L glucose, and 1 μCi D-[^{14}C(U)] glucose (PerkinElmer). A 2- × 2-cm Whatman 3M paper was taped on top of each well and wet with 100 μL 1 N NaOH. After incubation, filter-trapped $14CO_2$, medium-trapped $14CO_2$, and ^{14}C-labeled acid-soluble metabolites were determined by liquid scintillation counting in a Hidex 300 SL counter. Assays were performed in triplicate, and data were normalized to protein content.

Cell Transfections

HAP1-MDA5^{KO}RIG-I^{KO} and Huh7-RIG-I^{KO} cells were transfected with 1 μg DNA of pMDA5 or of pRIG-I, respectively, using Lipofectamine

2000 (Invitrogen) according to the manufacturer's protocol. After 24 hours, cells were trypsinized, and cell viability and ADP/ATP ratios were analyzed as described above. The expression of the plasmids was then confirmed by qRT-PCR. Poly-(I:C) was transfected in K422 cells using the Amaxa Nucleofector device. After 24 hours, cells were collected and subjected to quantitative RT-PCR for measuring gene expression of RIG-I and MDA5-coding genes, and to Western blot analysis for phosphorylated and total RIP1, cleaved and total caspase 3, and actin as described above.

Transmission Electron Microscopy

HBL1 cells were incubated with CM272 and venetoclax at IC_{50} doses, alone or in combination, for 24 hours. After prefixation in glutaraldehyde 0.5%, cells were pelleted and processed with a standard transmission electron microscopy protocol.

ECAR and OCR

ECAR and OCR were measured in an XF24 Extracellular flux analyzer (Seahorse Biosciences). After 24 hours of treatment of tumor cells, culture media were exchanged and replaced with XF base medium which modified DMEM (pH 7.4), 4 mmol/L Na-Pyruvate, and 2 mmol/L L-glutamine with or without 12.5 mmol/L glucose (for OCR or ECAR, respectively). Then, 2×10^5 cells were seeded in 2.5 μg/mL Cell-Tak precoated wells, centrifuged for 5 minutes at 300 × *g* at room temperature, and incubated for 30 minutes at 37°C without CO_2. ECAR and OCR were detected under basal conditions followed by the sequential injection of 12.5 mmol/L glucose, 2 μmol/L oligomycin, and 10 mmol/L 2-deoxyglucose for ECAR measurements or 2 μmol/L oligomycin, 4 μmol/L FCCP, 4 μmol/L antimycin A, and 1.5 μmol/L Rotenone for the OCR experiments. In addition, OCR was quantified with the fluorometric assay OCR-ST-96 Well Kit, according to the manufacturer's instructions.

Gas Chromatography/Mass Spectrometry for Metabolic Flux Analysis

Cells were cultured for 24 hours in the presence of fully labeled glucose or glutamine (^{13}C6-glucose or ^{13}C5-glutamine, Sigma-Aldrich). Then, cell pellets were scraped, collected, and frozen. Cell pellets were resuspended with 450 μL of cold methanol/water (8:1, v/v) containing ^{13}C-glycerol (5 ppm) as internal standard. Metabolite lysates were purified with three rounds of liquid nitrogen immersion and sonication, followed by 1 hour on ice before centrifugation (5,000 × *g*, 15 minutes at 4°C). Samples were dried under a stream of N_2 gas and lyophilized before chemical derivatization with 12 μL methoxyamine in pyridine (40 μg/μL) for 45 min at 60°C. Samples were also sialylated using 8 μL N-methyl-N-trimethylsilyltrifluoroacetamide with 1% trimethylchlorosilane (Thermo Fisher Scientific) for 30 minutes at 60°C to increase the volatility of metabolites. A 7890 GC system coupled to a 7000 QqQ mass spectrometer (Agilent Technologies) was used for isotopolog determination. Derivatized samples (1 μL) were injected into the gas chromatograph system with a split inlet equipped with a J&W Scientific DB5−MS+DG stationary phase column (30 mm × 0.25 mm i.d., 0.1 μmol/L film, Agilent Technologies). Helium was used as the carrier gas. Metabolites were ionized using positive chemical ionization with isobutene as reagent gas. Mass spectral data on the 7000 QqQ were acquired in scan mode, monitoring selected ion clusters of the various metabolites.

Fatty Acid Oxidation

Fatty acid oxidation was measured by the sum of $^{14}CO_2$ and ^{14}C-acid soluble metabolites. Briefly, after epigenetic treatment, cells (1×10^6) were incubated for 4 hours in Krebs-Ringer buffer without glucose. The medium was transferred to a glass vial with a central well containing benzethonium hydroxide (Sigma). $^{14}CO_2$ was liberated by acidification with 1 mol/L H_2SO_4 and collected during 2 hours in the central well. $^{14}CO_2$ was measured by scintillation counting in a scintillation counter Wallac 1409 (EG&G Company). Cells were washed and then scraped in cold buffer. Specific activity was measured and used to calculate total oxidation as equivalent of oxidized palmitic acid. Results were normalized to total protein content of cell extracts.

Glutamic Acid/Glutamate Uptake

After treatment, cells were washed twice with PBS and then preincubated for 1 hour in Krebs-modified buffer. Uptake assays were performed by incubating the cells for 15 minutes with 0.1 mmol/L L-glutamic acid and traces of L-[3,4-^{3}H]-glutamic acid (0.1 μCi/mL; Perkin Elmer). The reaction was stopped by adding 500 μL of cold PBS with calcium and magnesium (Sigma-Aldrich). Cells were washed 3 times with PBS and solubilized by adding 500 μL 1% Triton X-100 in 1 mol/L NaOH for 90 minutes at 37°C. Samples (100 μL) were taken to measure radioactivity by liquid scintillation counter. Protein concentration was determined by the Bradford method (Bio-Rad Protein Assay).

Measurement of Mitochondrial ROS Levels

Cells were grown in 96-well plates (10^5 cell/well) and treated with the corresponding drug for 24 hours. Prior to cell staining, control cells were treated with Antimycin A at 50 μmol/L for 30 minutes at 37°C. Then cells were stained with MitoSOX Red mitochondrial superoxide indicator reagent at 2.5 μmol/L concentration for 30 minutes at 37°C (Thermo Fisher Scientific). Cells were washed twice in PBS and stained with ToPro3 as dead cell indicator (Invitrogen) at 1 μmol/L concentration for 5 minutes at room temperature. Finally, ROS levels were measured by flow cytometry using a FACSCantoII (BD Biosciences).

Enzymatic Activity Assays

Enzymatic activity of ETC complexes I (NADH dehydrogenase), II (SDH), III (cytochrome c reductase), IV (cytochrome c oxidase), V (ATP synthase complex), PDH, and GLUD1 was measured using commercial kits listed in the Key Resources Table in the Supplementary Material. Briefly, treated cells were washed with PBS, lysed (1% Triton-X-100 and 1 mmol/L DTT in PBS) for 10 minutes on ice, and centrifuged at 700 × *g* for 10 minutes at 4°C. Protein concentration was quantified with BCA, and the enzymatic activities were measured using specific colorimetric kits, according to the manufacturer's instructions.

Measurement of Mitochondrial Membrane Potential

TMRE fluorescence labeling was used to detect changes in $\Delta\Psi_{mito}$. After treatment with the corresponding drug, 100 nmol/L TMRE was added to the culture medium and then incubated in the dark for 30 minutes at 37°C in 5% CO_2. A control of total mitochondrial membrane depolarization was included treating in parallel cells with 20 μmol/L FCCP for 10 minutes. The fluorescence intensity (Ex/Em, 549/575 nm) was quantified using Skanit Varioskan Flash 2.4.3 (Thermo Fisher Scientific).

In Vivo Therapy

All mouse experiments were performed in the Animal Core Facilities of the Center for Applied Medical Research after approval by the University of Navarra Animal Ethics Committee. 5×10^6 tumor K422, HBL1, or MM1S cells in PBS with Matrigel (1:1 ratio) were injected s.c. into immunodeficient $Rag2^{-/-}IL2\gamma c^{-/-}$ 8-week-old female mice (The Jackson Laboratory). Tumor inoculations and therapies were performed as previously reported (54). Briefly, once tumor volumes reached 100 to 150 mm^3, mice were randomly divided into four groups: untreated control, treated with CM272, treated with proapoptotic drug (venetoclax or S63845), and treated with CM272 and the proapoptotic drug. Venetoclax or S63845 were administrated i.p. twice per week (50 mg/kg in DMSO), whereas CM272 (2.5 mg/kg in PBS) was administered i.p. for 5 consecutive days per week. Treatment was administered for 2 weeks. Tumor growth was monitored by measuring tumor size in two orthogonal dimensions by caliper measurement.

Statistical Analyses

Analysis for evaluation of the antitumor effect of drug combinations was performed using the software of CompuSyn (ComboSyn, Inc.). The average of the CI value was plotted using the GraphPad Prism version v.7.0 (GraphPad Software Inc.). A synergistic effect between two drugs was considered when at least four different drug–drug interactions showed CI < 1. All statistical analyses were performed using GraphPad Prism 7.0. Two-tailed Student t test or Mann–Whitney U test was used for evaluating statistically significant differences of gene expression values. Statistical significance was indicated as follows: *, $P < 0.05$; **, $P < 0.01$; ***, $P < 0.001$; n.s., not significant.

Authors' Disclosures

V. Fresquet reports a patent for Dual inhibitors against G9a/DNMT issued. C. Vicente reports grants from Spanish Association Against Cancer (AECC) during the conduct of the study. C. Panizo reports grants and personal fees from Roche Parma and other support from Bristol-Myers Squibb and Kyowa Kirin outside the submitted work. J. Han reports grants from Xiamen University, China, during the conduct of the study. R. Pio reports grants and personal fees from Amadix and grants from AstraZeneca outside the submitted work. J. Oyarzabal reports a patent for Dual inhibitors against G9a/DNMT issued. B. Paiva reports other support from Amgen, Adaptive, and Janssen, grants and other support from BMS-Celgene; grants and other support from Sanofi and Takeda; and grants from Roche outside the submitted work. F. Prosper reports grants from ISCIII-Feder Funds and Government of Navarra during the conduct of the study; in addition, F. Prosper has a patent for Dual Inhibitors against G9a/DNMT issued. J.A. Martinez-Climent reports grants from Spanish Ministry of Health during the conduct of the study; in addition, J.A. Martinez-Climent has a patent for Dual Inhibitors against G9a/DNMT issued. No disclosures were reported by the other authors.

Authors' Contributions

V. Fresquet: Conceptualization, formal analysis, supervision, validation, investigation, methodology, writing–original draft, writing–review and editing. **A. Junza:** Investigation, methodology. **J. Han:** Resources. **C. Prior:** Investigation. **P. Fortes:** Investigation, writing–review and editing. **R. Pio:** Resources, investigation, writing–review and editing. **J. Oyarzabal:** Resources. **A. Martinez-Baztan:** Investigation. **B. Paiva:** Resources, investigation, writing–review and editing. **M.J. Moreno-Aliaga:** Resources, investigation, writing–review and editing. **M.D. Odero:** Resources, investigation, writing–review and editing. **M.J. Garcia-Barchino:** Formal analysis, validation, investigation, methodology, writing–review and editing. **X. Agirre:** Investigation, writing–review and editing. **O. Yanes:** Resources, investigation, methodology, writing–review and editing. **F. Prosper:** Conceptualization, resources, investigation, writing–review and editing. **J.A. Martinez-Climent:** Conceptualization, resources, formal analysis, supervision, funding acquisition, validation, investigation, visualization, methodology, writing–original draft, project administration, writing–review and editing. **M.J. Larrayoz:** Resources. **J. Celay:** Formal analysis, validation, investigation, methodology, writing–review and editing. **C. Vicente:** Validation, investigation, methodology, writing–review and editing. **M. Fernandez-Galilea:** Formal analysis, investigation, visualization, methodology. **M. Larrayoz:** Formal analysis, validation, investigation, methodology, writing–review and editing. **M.J. Calasanz:** Resources. **C. Panizo:** Resources, writing–review and editing.

Acknowledgments

The authors thank Bart Bartenschlager (University of Heidelberg) for providing Huh7 MAVS KO cells, Edurne San Jose Eneriz, Asun Redin, and Rosa Castilla-Madrigal for technical assistance, Eneko Elizalde and Elena Ciordia for animal care, Luis Montuenga for providing lung cancer primary samples, Ricardo Andrade and SGIker for technical and human support, and the University of Navarra Biobank for handling samples from patients with hematologic malignancies. This work was supported by Instituto de Salud Carlos III (FIS) and co-supported by FEDER (Spanish Ministry of Health) grants PI19/00818 (to J.A. Martinez-Climent), PI17/00411 (to R. Pio), PI17/02272 (to M.D. Odero), PI19/01352 (to X. Agirre), PI17/00701 (to F. Prosper), and ERA-NET EPICA AC16/00041 (to F. Prosper); by CIBERONC #CB16/12/00489 (to C. Panizo, M.D. Odero, X. Agirre, F. Prosper, and J.A. Martinez-Climent), #CB16/12/00369 (to B. Paiva), and #CB16/12/00443 (to R. Pio); by CIBEROBN #CB12/03/30002 (to M.J. Moreno-Aliaga); by CIBERDEM #CB07/08/0014 (to A. Junza and O. Yanes); by CIBEREHD #CB06/04/0006 (to P. Fortes); by the Spanish Ministry of Science and Innovation grants RTI2018-101759-B-I00 (to P. Fortes), PID2019-106982RB-I00 (to M.J. Moreno-Aliaga), and BFU2017-87958-P (to O. Yanes); by Government of Navarra/FEDER GNS-2016-XA (to X. Agirre); by PerMed 2019 MEET-AML (to F. Prosper); by MMRF 2017 Immunotherapy Program Grant Award (to F. Prosper); and by the AECC (to R. Pio). V. Fresquet was supported by FIS–Spanish Ministry of Health. M.J. Garcia-Barchino was supported by Fundacion Arnal Planelles. M. Larrayoz, J. Celay, and M. Fernandez-Galilea were supported by the Spanish Ministry of Science and Innovation through "Juan de la Cierva" grants. M. Larrayoz and C. Vicente were supported by junior investigator grants from AECC. J. Celay was supported by AECC through an "Accelerator" grant. A. Martinez-Baztan was supported by a predoctoral grant from CIMA/University of Navarra.

Received July 21, 2020; revised October 8, 2020; accepted December 14, 2020; published first December 18, 2020.

REFERENCES

1. Jones PA, Issa JP, Baylin S. Targeting the cancer epigenome for therapy. Nat Rev Genet 2016;17:630–41.
2. Berdasco M, Esteller M. Clinical epigenetics: seizing opportunities for translation. Nat Rev Genet 2019;20:109–27.
3. Roulois D, Loo Yau H, Singhania R, Wang Y, Danesh A, Shen SY, et al. DNA-demethylating agents target colorectal cancer cells by inducing viral mimicry by endogenous transcripts. Cell 2015;162:961–73.
4. Chiappinelli KB, Strissel PL, Desrichard A, Li H, Henke C, Akman B, et al. Inhibiting DNA methylation causes an interferon response in cancer via dsRNA including endogenous retroviruses. Cell 2015; 162:974–86.
5. Kassiotis G, Stoye JP. Immune responses to endogenous retroelements: taking the bad with the good. Nat Rev Immunol 2016;16:207–19.
6. Ohtani H, Liu M, Zhou W, Liang G, Jones PA. Switching roles for DNA and histone methylation depend on evolutionary ages of human endogenous retroviruses. Genome Res 2018;28:1147–57.
7. Deniz Ö, Frost JM, Branco MR. Regulation of transposable elements by DNA modifications. Nat Rev Genet 2019;20:417–31.
8. Brocks D, Schmidt CR, Daskalakis M, Jang HS, Shah NM, Li D, et al. DNMT and HDAC inhibitors induce cryptic transcription start sites encoded in long terminal repeats. Nat Genet 2017;49:1052–60.
9. Liu M, Thomas SL, DeWitt AK, Zhou W, Madaj ZB, Ohtani H, et al. Dual inhibition of DNA and histone methyltransferases increases viral mimicry in ovarian cancer cells. Cancer Res 2018;78:5754–66.
10. Stone ML, Chiappinelli KB, Li H, Murphy LM, Travers ME, Topper MJ, et al. Epigenetic therapy activates type I interferon signaling in murine ovarian cancer to reduce immunosuppression and tumor burden. Proc Natl Acad Sci U S A 2017;114:E10981–E90.
11. Topper MJ, Vaz M, Chiappinelli KB, DeStefano Shields CE, Niknafs N, Yen RC, et al. Epigenetic therapy ties MYC depletion to reversing immune evasion and treating lung cancer. Cell 2017;171:1284–300.
12. Sheng W, LaFleur MW, Nguyen TH, Chen S, Chakravarthy A, Conway JR, et al. LSD1 ablation stimulates anti-tumor immunity and enables checkpoint blockade. Cell 2018;174:549–63.

13. Jones PA, Ohtani H, Chakravarthy A, De Carvalho DD. Epigenetic therapy in immune-oncology. Nat Rev Cancer 2019;19:151–61.
14. Topper MJ, Vaz M, Marrone KA, Brahmer JR, Baylin SB. The emerging role of epigenetic therapeutics in immuno-oncology. Nat Rev Clin Oncol 2020;17:75–90.
15. San José-Enériz E, Agirre X, Rabal O, Vilas-Zornoza A, Sanchez-Arias JA, Miranda E, et al. Discovery of first-in-class reversible dual small molecule inhibitors against G9a and DNMTs in hematological malignancies. Nat Commun 2017;8:15424.
16. Segovia C, San José-Enériz E, Munera-Maravilla E, Martínez-Fernández M, Garate L, Miranda E, et al. Inhibition of a G9a/DNMT network triggers immune-mediated bladder cancer regression. Nat Med 2019;25:1073–81.
17. Tormo D, Checińska A, Alonso-Curbelo D, Pérez-Guijarro E, Cañón E, Riveiro-Falkenbach E, et al. Targeted activation of innate immunity for therapeutic induction of autophagy and apoptosis in melanoma cells. Cancer Cell 2009;16:103–14.
18. Besch R, Poeck H, Hohenauer T, Senft D, Häcker G, Berking C, et al. Proapoptotic signaling induced by RIG-I and MDA-5 results in type I interferon-independent apoptosis in human melanoma cells. J Clin Invest 2009;119:2399–411.
19. Marks PA, Breslow R. Dimethyl sulfoxide to vorinostat: development of this histone deacetylase inhibitor as an anticancer drug. Nat Biotechnol 2007;25:84–90.
20. Kato H, Takeuchi O, Sato S, Yoneyama M, Yamamoto M, Matsui K, et al. Differential roles of MDA5 and RIG-I helicases in the recognition of RNA viruses. Nature 2006;441:101–5.
21. Hou F, Sun L, Zheng H, Skaug B, Jiang QX, Chen ZJ. MAVS forms functional prion-like aggregates to activate and propagate antiviral innate immune response. Cell 2011;146:448–61.
22. Singh R, Letai A, Sarosiek K. Regulation of apoptosis in health and disease: the balancing act of BCL-2 family proteins. Nat Rev Mol Cell Biol 2019;20:175–93.
23. Vanden Berghe T, Linkermann A, Jouan-Lanhouet S, Walczak H, Vandenabeele P. Regulated necrosis: the expanding network of non-apoptotic cell death pathways. Nat Rev Mol Cell Biol 2014;15:135–47.
24. Yao H, Dittmann M, Peisley A, Hoffmann HH, Gilmore RH, Schmidt T, et al. ATP-dependent effector-like functions of RIG-I-like receptors. Mol Cell 2015;58:541–8.
25. Peisley A, Lin C, Wu B, Orme-Johnson M, Liu M, Walz T, et al. Cooperative assembly and dynamic disassembly of MDA5 filaments for viral dsRNA recognition. Proc Natl Acad Sci U S A 2011;108:21010–5.
26. Leist M, Single B, Castoldi AF, Kühnle S, Nicotera P. Intracellular adenosine triphosphate (ATP) concentration: a switch in the decision between apoptosis and necrosis. J Exp Med 1997;185:1481–6.
27. Nistal-Villán E, Gack MU, Martínez-Delgado G, Maharaj NP, Inn KS, Yang H, et al. Negative role of RIG-I serine 8 phosphorylation in the regulation of interferon-beta production. J Biol Chem 2010;285:20252–61.
28. Bamming D, Horvath CM. Regulation of signal transduction by enzymatically inactive antiviral RNA helicase proteins MDA5, RIG-I, and LGP2. J Biol Chem 2009;284:9700–12.
29. Vander Heiden MG, Cantley LC, Thompson CB. Understanding the Warburg effect: the metabolic requirements of cell proliferation. Science 2009;324:1029–33.
30. Wang X, Jiang W, Yan Y, Gong T, Han J, Tian Z, et al. RNA viruses promote activation of the NLRP3 inflammasome through a RIP1-RIP3-DRP1 signaling pathway. Nat Immunol 2014;15:1126–33.
31. Zhang DW, Shao J, Lin J, Zhang N, Lu BJ, Lin SC, et al. RIP3, an energy metabolism regulator that switches TNF-induced cell death from apoptosis to necrosis. Science 2009;325:332–6.
32. Yang Z, Wang Y, Zhang Y, He X, Zhong CQ, Ni H, et al. RIP3 targets pyruvate dehydrogenase complex to increase aerobic respiration in TNF-induced necroptosis. Nat Cell Biol 2018;20:186–97.
33. Cantor JR, Sabatini DM. Cancer cell metabolism: one hallmark, many faces. Cancer Discov 2012;2:881–98.
34. Shadel GS, Horvath TL. Mitochondrial ROS signaling in organismal homeostasis. Cell 2015;163:560–9.
35. Nunnari J, Suomalainen A. Mitochondria: in sickness and in health. Cell 2012;148:1145–59.
36. Birsoy K, Possemato R, Lorbeer FK, Bayraktar EC, Thiru P, Yucel B, et al. Metabolic determinants of cancer cell sensitivity to glucose limitation and biguanides. Nature 2014;508:108–12.
37. Ashkenazi A, Fairbrother WJ, Leverson JD, Souers AJ. From basic apoptosis discoveries to advanced selective BCL-2 family inhibitors. Nat Rev Drug Discov 2017;16:273–84.
38. Kotschy A, Szlavik Z, Murray J, Davidson J, Maragno AL, Le Toumelin-Braizat G, et al. The MCL1 inhibitor S63845 is tolerable and effective in diverse cancer models. Nature 2016;538:477–82.
39. Chonghaile TN, Roderick JE, Glenfield C, Ryan J, Sallan SE, Silverman LB, et al. Maturation stage of T-cell acute lymphoblastic leukemia determines BCL-2 versus BCL-XL dependence and sensitivity to ABT-199. Cancer Discov 2014;4:1074–87.
40. Leverson JD, Phillips DC, Mitten MJ, Boghaert ER, Diaz D, Tahir SK, et al. Exploiting selective BCL-2 family inhibitors to dissect cell survival dependencies and define improved strategies for cancer therapy. Sci Transl Med 2015;7:279ra40.
41. Pollyea DA, Stevens BM, Jones CL, Winters A, Pei S, Minhajuddin M, et al. Venetoclax with azacitidine disrupts energy metabolism and targets leukemia stem cells in patients with acute myeloid leukemia. Nat Med 2018;24:1859–66.
42. DiNardo CD, Jonas BA, Pullarkat V, Thirman MJ, Garcia JS, Wei AH, et al. Azacitidine and venetoclax in previously untreated acute myeloid leukemia. N Engl J Med 2020;383:617–29.
43. Cuellar TL, Herzner AM, Zhang X, Goyal Y, Watanabe C, Friedman BA, et al. Silencing of retrotransposons by SETDB1 inhibits the interferon response in acute myeloid leukemia. J Cell Biol 2017;216:3535–49.
44. Mehdipour P, Marhon SA, Ettayebi I, Chakravarthy A, Hosseini A, Wang Y, et al. Epigenetic therapy induces transcription of inverted SINEs and ADAR1 dependency. Nature 2020;588:169–73.
45. Levine AJ, Puzio-Kuter AM. The control of the metabolic switch in cancers by oncogenes and tumor suppressor genes. Science 2010;330:1340–4.
46. Koppenol WH, Bounds PL, Dang CV. Otto Warburg's contributions to current concepts of cancer metabolism. Nat Rev Cancer 2011;11:325–37.
47. Moskowitz AJ, Horwitz SM. Targeting histone deacetylases in T-cell lymphoma. Leuk Lymphoma 2017;58:1306–19.
48. San-Miguel JF, Hungria VT, Yoon SS, Beksac M, Dimopoulos MA, Elghandour A, et al. Panobinostat plus bortezomib and dexamethasone versus placebo plus bortezomib and dexamethasone in patients with relapsed or relapsed and refractory multiple myeloma: a multicentre, randomised, double-blind phase 3 trial. Lancet Oncol 2014;15:1195–206.
49. Montalban-Bravo G, Garcia-Manero G. Myelodysplastic syndromes: 2018 update on diagnosis, risk-stratification and management. Am J Hematol 2018;93:129–47.
50. Morel D, Jeffery D, Aspeslagh S, Almouzni G, Postel-Vinay S. Combining epigenetic drugs with other therapies for solid tumours - past lessons and future promise. Nat Rev Clin Oncol 2020;17:91–107.
51. Bender S, Reuter A, Eberle F, Einhorn E, Binder M, Bartenschlager R. Activation of type I and III interferon response by mitochondrial and peroxisomal MAVS and inhibition by hepatitis C virus. PLoS Pathog 2015;11:e1005264.
52. Blight KJ, McKeating JA, Rice CM. Highly permissive cell lines for subgenomic and genomic hepatitis C virus RNA replication. J Virol 2002;76:13001–14.
53. Beltran E, Fresquet V, Martinez-Useros J, Richter-Larrea JA, Sagardoy A, Sesma I, et al. A cyclin-D1 interaction with BAX underlies its oncogenic role and potential as a therapeutic target in mantle cell lymphoma. Proc Natl Acad Sci U S A 2011;108:12461–6.
54. Fresquet V, Rieger M, Carolis C, Garcia-Barchino MJ, Martinez-Climent JA. Acquired mutations in BCL2 family proteins conferring resistance to the BH3 mimetic ABT-199 in lymphoma. Blood 2014;123:4111–9.